STRUCTURE AND BEHAVIOR OF THE Ni END-MEMBER SCHREIBERSITE, (Ni$_3$P), UNDER DEEP EARTH CONDITIONS

A THESIS SUBMITTED TO THE GRADUATE DIVISION OF THE
UNIVERISTY OF HAWAI'I AT MĀNOA IN PARTIAL FULFILLMENT OF
THE REQUIREMENTS FOR THE DEGREE OF

MASTER OF SCIENCE

IN

GEOLOGY AND GEOPHYSICS

MAY 2019

By

SASITHORN CHORNKRATHOK

Thesis Committee:

Przemyslaw Dera, Chairperson
Bin Chen
Patricia Fryer

Keywords: Schreibersite, High pressure, Diamond Anvil Cell, Synchrotron X-ray diffraction,
Single-crystal X-ray diffraction, Crystallography

Acknowledgements

I would like to take this opportunity to express my gratitude to everyone who has supported me throughout my thesis research as a master student at the University of Hawaiʻi at Mānoa. I would first offer my utmost gratitude to my thesis advisor Dr. Przemyslaw Dera, for his valuable advice, supervision and crucial contribution to this thesis. He not only opened my perspective in crystallography, especially in the high-pressure field, but he also supported and helped me during my experiments in Chicago. The door to his office was always open whenever I ran into a trouble spot or had a question about my research or writing. He consistently allowed this paper to be my own work but steered me in the right the direction whenever he thought I needed it. It has been an absolute pleasure working with him for almost two years. I am eternally grateful for it.

Besides my advisor, I would like to thank the rest of my thesis committee: Dr. Bin Chen and Dr. Patricia Fryer, for their insightful comments and encouragement, but also for the hard question which incentivized me to widen my research from various perspectives.

I thank my research group, Dr. Gregory Finkelstein, Dr. Hannah Shelton, Dr. Dongzhou Zhang, Dr. Yi Hu and Tommy Yong for their unfailing advice and assistance as colleagues and friends in my master's student life both in Hawaii and Chicago.

I express my thanks the support from Development and Promotion of Science and Technology Talents Project (DPST) graduate scholarship awarded by the government of Thailand, Department of Earth Sciences (formerly known as Geology and Geophysics), and Hawaiʻi Institute of Geophysics and Planetology at the University of Hawaiʻi at Mānoa

Finally, I must express my very profound gratitude to my parents and to my sister for providing me with support and continuous encouragement throughout my years of study. This accomplishment would not have been possible without them. Thank you very much.

Abstract

Earth's core is believed to be primarily composed of iron-nickel (Fe-Ni) alloy, however, observed seismic velocities suggest the presence of an appreciable amount of one or more light elements. Among several other alloys and compounds, Fe-Ni phosphides are considered as candidates for minor core phases and would have the effect of lowering the core density. While Fe-phosphides have been the subject of earlier experimental and computational studies, the effects of Ni, the second major element in the core, have not been systematically investigated. This project focuses on the investigation of the crystal structure and behavior of the most metal-rich of Ni-P binary compounds, the Ni end-member schreibersite (Ni_3P), using synchrotron X-ray diffraction (XRD) experiments. Ni_3P is isostructural with Fe_3P and has a tetragonal symmetry with $I\bar{4}$ space group. In our experiments both powder and two single crystal samples of synthetic Ni_3P in different orientations, with respect to the axis of the diamond anvil cell, were compressed up to approximately 50 gigapascals (GPa) at ambient temperature. The compressional data of Ni_3P were fitted by the 3rd order Birch–Murnaghan equation of state, and yielded $V_0 = 351.44(8)$ $Å^3$, $K_{T0} =$ 190(4) GPa, $K' = 4.9(4)$ for powder data below 35 GPa, $K_{T0} = 199(5)$ GPa, $K'=4.7(4)$ for single-crystal 1 data below 30 GPa, and $K_{T0} = 194(5)$ GPa, $K' = 4.7(8)$ for single crystal 2 below 25 GPa. All data suggest that at low pressure (~< 30 GPa), the c/a ratio of unit cell parameters remains approximately constant, but they start to increase steadily above that pressure and experience a second slight discontinuity at approximately 40 GPa. The change in unit cell parameters at ~30 GPa and ~40 GPa suggests discontinuous changes in magnetic ordering. Moreover, the threshold of these subtle discontinuities is sensitive to the stress state and orientation of the crystal in the diamond anvil cell. This study is the first report of compressional behavior of both powder and single crystal Ni_3P up to 50 GPa and offers insights into the effects of Ni_3P components on the compressional behavior of schreibersite in the Earth's core.

Table of Contents

List of Figures

List of Tables

1. Introduction

1.1 Possible importance of compounds of iron, nickel and light elements in the Earth's core.

The knowledge of chemical composition and physical properties of the Earth's interior mostly comes from seismic observations, geophysical modeling, from direct observation of surface rocks, and the study of meteorites (McDonough & Sun, 1995; Allègre et al., 1995; Litasov & Shatskiv, 2016). Unfortunately, at present, Earth's deep interior cannot be directly sampled due to engineering limitations, as the deepest hole that has been drilled thus far reached only approximately 12 kilometers (Kozlovsky, 1984). Experimental investigations at high pressures and high temperatures have been playing an important role in studying the Earth's interior. According to current understanding, the Earth interior can be divided into five main regions: crust, upper mantle, lower mantle, outer core, and inner core (e.g., Ringwood, 1977; Anderson, 1989; McDonough & Sun, 1995; Allègre et al., 1995; McDonough, 2014; Litasov & Shatskiv, 2016) as shown in Figure 1 and Table 1.
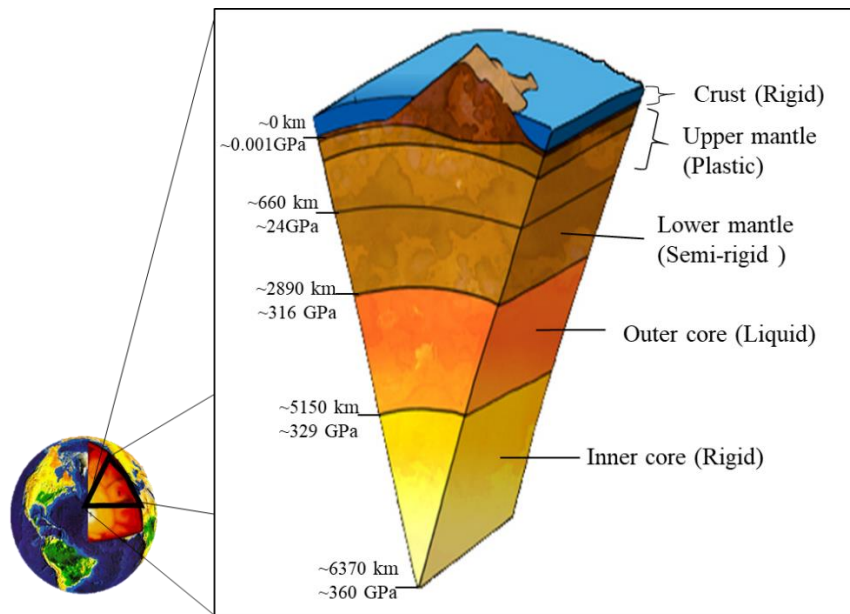
Figure 1. The structure of the Earth's interior (modified from mstworkbooks/ natural-sciences/).

1

Table 1. The chemical composition and physical properties of the Earth.

layer	Depth (km)	Pressure (GPa)	Temperature (℃)	Physical property	Main type of rocks, minerals and chemical composition
surface — 0 km					
Crust		0.0001-1 GPa	-89.2-870 ℃	Solid (Rigid)	Silicate rock
——— 10-70 km					
Upper mantle		13-24 GPa	200-900 ℃	Solid (partially fluid)	Olivine, pyroxene and garnet
——— ~660 km					
Lower mantle		25-136 GPa	1600-4000 ℃	Semi-rigid	Mg, Fe-perovskite, Ca-perovskite and (Mg, Fe)O
——— ~2890 km					
Outer core		150-329 GPa	4400-5500 ℃	Liquid (Low-viscosity fluid)	Fe, Ni, Co, Cr and light elements
——— ~5150 km					
Inner core		330-360 GPa	5400-6700 ℃	Solid	Fe, Ni, and light elements
——— ~6370 km					

Iron-nickel (Fe-Ni) alloy, which consists of iron, nickel and light elements (sulfur, phosphorus, oxygen, etc.) is believed to be present in the Earth's core (Birch, 1952; McDonough & Sun, 1995; Allègre et al., 1995; Litasov & Shatskiv, 2016). Based on seismic evidence, we know that the density of Earth's core is approximately 10 % lower than the density of pure Fe at core pressure and temperature (e.g. Birch, 1952; Allègre et al., 1995; Li & Fei, 2003) (Figure 2). The current interpretation of this density deficit involves the presence of a significant amount of nickel, along with small (up to 10%) amounts of one or several light elements such as sulfur, phosphorus, oxygen, silicon, hydrogen, carbon, and potassium (McDonough & Sun, 1995; Poirier, 1994; Litasov & Shatskiv, 2016). In addition to decreasing density, the presence of Fe-Ni alloys with light elements affects elastic properties and acoustic wave velocities. For example, Fe-silicon alloy

increases both compressional and shear wave velocity, whereas adding Ni in Fe-compounds decreases the compressional wave velocity and shear wave velocity (Lin et al., 2003). In order to understand the evolution and formation of the Earth's core in terms of discrete physical phenomena, experimentally measured elasticity and other physical properties of potential alloys present in the Earth's core are required.
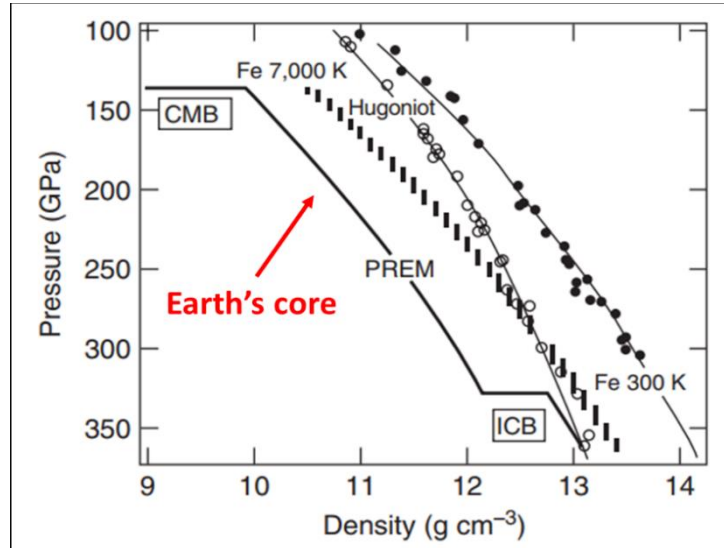
Figure 2. The difference between the density of pure iron and that of Preliminary Reference Earth Model (PREM). The density of Earth's core is approximately 10 % lower than the density of pure Fe at core pressure and temperature (Li & Fei, 2003).

Among light elements suspected to be present in the core, phosphorus (P) is particularly interesting, because of its importance for life. P is present in the structure of living cells, helps to carry genetic information, is part of DNA, the fundamental building blocks of life, and contributes to ATP, the energy currency of life (Maciá et.al., 1997; Bryant et al., 2013). Although estimated concentration of P in the core is rather low (~0.2 %) (McDonough, 2014; Litasov & Shatskiv, 2016), phosphide minerals, especially Fe-Ni-P alloys that are found in iron-meteorites, such as iron monophosphide (FeP) (Gu et al., 2011), nickel monophosphide (NiP) (Dera et al., 2011a), allabogdanite ($(Fe,Ni)_2P$ (orthorhombic)) (Britvin et al., 2002), barringerite ($(Fe,Ni)_2P$)

3

(hexagonal)) (Brandstätter et al., 1911; Buseck, 1969; Dera et al., 2009), schreibersite ((Fe,Ni)$_3$P (tetragonal)) (Geist et al., 2005; Scott et al., 2007), nickel-phosphide ((Ni,Fe)$_3$P) (tetragonal)) (Britvin et al., 1999, Skála & Drábek, 2003), or melliniite ((Ni,Fe)$_4$P) (Pratesi et al., 2006), have long been studied to investigate the formation of planetary bodies.

1.2 Introduction to schreibersite

Natural schreibersite is an iron-nickel phosphide [(Fe, Ni)$_3$P], and occurs as a minor mineral phase in iron and stony-iron meteorites (Geist et al., 2005). Meteoritic schreibersite usually has higher Fe than Ni content. Compositions with Ni content greater than 50% are called nickel phosphide (Skála & Drábek, 2003). Schreibersite forms a solid solution between Fe$_3$P and Ni$_3$P. It has a metallic luster, a density of 7.0-7.3 g/cm^3 and hardness of 6.5-7 on the Mohs hardness scale. It forms tetragonal crystals with perfect 001 cleavage and non-centrosymmetric space group $I\bar{4}$ (Skála & Císařová, 2005). In the unit cell, there are four atomic positions in crystallographically non-equivalent 8g Wyckoff sites with the coordinates of (x, y, z), ($\frac{1}{2}$x, $\frac{1}{2}$y, $\frac{1}{2}$z), (-x, -y, z), (-$\frac{1}{2}$x, -$\frac{1}{2}$y, $\frac{1}{2}$z), (y, -x, -z), ($\frac{1}{2}$y, -$\frac{1}{2}$x, -$\frac{1}{2}$z), (-y, x, -z), (-$\frac{1}{2}$y, $\frac{1}{2}$x, -$\frac{1}{2}$z). Three of them are occupied by a metallic atom (Fe, Ni) and another one is P atom (Skála & Císařová, 2005; Pritekel, 2015). The unit cell parameters of Fe$_3$P (Rundquist, 1962; Scott et al., 2007; Gu et al., 2014) and Ni$_3$P (Aronsson, 1955; Rundqvist et al., 1962; Jun et al., 2007) are shown in Table 2, and Figure 3. At ambient conditions, Fe$_3$P and Ni$_3$P schreibersite end-members are Pauli paramagnets (Gambino et al., 1967; Zeppenfeld & Jeitschko, 1993). Pauli paramagnetism is a tendency of the spins of delocalized free electrons in the metal atoms to transfer from antiparallel to parallel states in the presence of an external magnetic field.

Table 2. Crystal structure of end-member schreibersite at ambient pressure and temperature (Numbers in parentheses represent errors in the last digit).

	Space Group	a (Å)	c (Å)	Bond distance (Å)
Fe$_3$P	$I\bar{4}$	9.103(4)	4.464(5)	Fe-P (2.31 Å -3.59 Å), Fe-Fe (2.41 Å -3.53 Å)
Ni$_3$P	$I\bar{4}$	8.952(2)	4.388(2)	Ni-P (2.21 Å -2.35 Å), Ni-Ni (2.43 Å -2.86 Å)
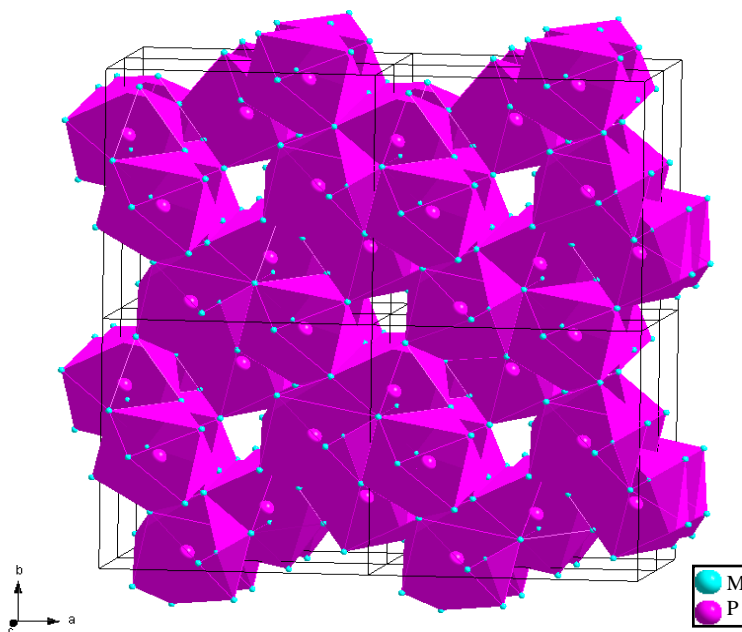
Figure 3. The tetragonal structure of schreibersite. M represent three metallic atom sites (Fe and Ni). P is phosphorus site.

Disko Island in Greenland is the only place on the Earth where natural schreibersite has been found in basalt lenses (Pedersen, 1981; Ulff-Møller, 1985). Although occurrences of schreibersite on the Earth's surface are rare, the implications of possible schreibersite existence in the deep interior might be important for the origin of life on Earth (Bryant et al., 2013). It is believed that meteoritic phosphide minerals including schreibersite could have been one of the primary sources of phosphorus on early Earth (Pasek & Lauretta, 2005; Board et al., 2007; Gull et al., 2015).

1.3 Schreibersite at high pressure

Studying minerals through high-pressure and temperature experiments has allowed us to see how crystals respond to the external forces that act on rocks at depth. There have been numerous previous studies investigating the alloys between Fe, Ni, and light elements, however, the main research has focused on Fe-rich compounds, because Fe is the major element in the core. Pure Fe is stable in hexagonal close packed (hcp) structure above ~10 GPa at 300 K (Hemley & Mao, 2001; Kuwayama et al., 2008), while Pure Ni is stable in face-centered cubic (fcc) structure at high pressure (Huang et al., 1988; Lin et al., 2002; Mao et al., 2006). Alloying iron and nickel lead to stabilization of the fcc phase at high pressure and low temperature (Lin et al., 2002; Kuwayama et al., 2008; Mao et al., 2006). Another interesting observation is that the value of the axial ratio (c/a) of the hcp-Fe phase is lower than theoretically estimated, which has an effect on the longitudinal anisotropy of the hcp phase and might influence the seismic anisotropy of the Earth's core (Steinle-Neumann et al., 2001; Lin et al., 2002).

Due to the possibility of forming alloys and solid compounds between Fe and light elements, a lot of research has been devoted to studying stability, physical properties and behavior of such phases, including schreibersite Fe end-member, Fe_3P, (e.g. Scott et al., 2007; Howard, 2010; Gu et al., 2014), as well as the isostructural Fe_3S (e.g., Fei et al., 2000; Lin et al., 2004; Seagle et al, 2006; Kamada et al., 2010). Intriguing discontinuous behavior has been reported in Fe_3P, including for example *a* change in c/a ratio on compression, attributed to magnetic ordering transition (Gu et al., 2014). The formation of a non-quenchable high-temperature phase was found above 1600 K at 64 GPa (Gu et al., 2014). In the isostructural Fe_3S, a magnetic collapse was found at 21 GPa. The disordered magnetic moment affects the elasticity and thermodynamics of Fe_3S (Lin et al., 2004). Moreover, Fe_3S is stable up to 220 GPa and 3300 K (Kamada et al., 2010).

Despite that the Earth's core mainly consists of Fe, the effects of Ni, the second major element in the core, may be very important but have not been systematically investigated. Constraining the properties of the Ni end-member schreibersite is important for understanding schreibersite's reactivity, as well as crucial for proper modeling of solid solution phases with intermediate Fe/Ni ratios consistent with meteorites. Thus, this project focuses on the investigation of the crystal structure and behavior of Ni end-member schreibersite (Ni_3P) at high pressures using synchrotron powder X-ray diffraction and synchrotron single crystal X-ray diffraction in a diamond anvil cell with full crystallographic analysis of results, including unit cell parameter, structure refinements, and determination of equations of state. Better understanding of the effects of the potential presence of light element alloys of Fe and Ni, such as schreibersite, will provide new constraints on the evolution and formation of the Earth, and also be helpful for studying the core of other planet or moons.

2. Experimental methods

2.1 Sample synthetic and characteristics

The Ni_3P compound used in all our studies was synthesized by Dr. Nabil Boctor, our collaborator at Carnegie Institution of Science, from a stoichiometric mixture of Ni and P elements with a molar ratio of 3:1 in a silica tube in a high-temperature furnace at 1000 °C.

The synthetic Ni_3P was measured for presence of secondary minor elements by using micro X-Ray Fluorescence (XRF). We used a custom XRF spectrometer with an energy-dispersive detector to measure specific excitation peaks for each element. The X-ray fluorescence phenomenon relies on the principle that all atoms absorb the X-ray photons by ejecting the electron from a low energy level (K or L) and replacing it with the electron from a higher energy level in

an outer orbital. During the ejection, energy is released due to decrease of the energy in the inner orbital. The released energy is in the form of characteristic X-rays, indicating the type of atom present. The XRF spectra for this project were collected with an Amptek X123 SSD Fast detector (Figure 4) using the DPPMCA program. The resulting spectra were analyzed with the PyMCA program (Solé & Papillon, 2004). The instrument that we used for analyses did not have a vacuum enclosure, and air present between the sample and the detector absorbed most of the low-energy P K_α peak (2.015 keV). The XRF spectrum of the synthetic Ni_3P is shown in Figure 5. The only well-defined peaks are Ni K_α (7.477 KeV) and Ni K_β (8.264 KeV), which is consistent with the end-member composition of the sample.
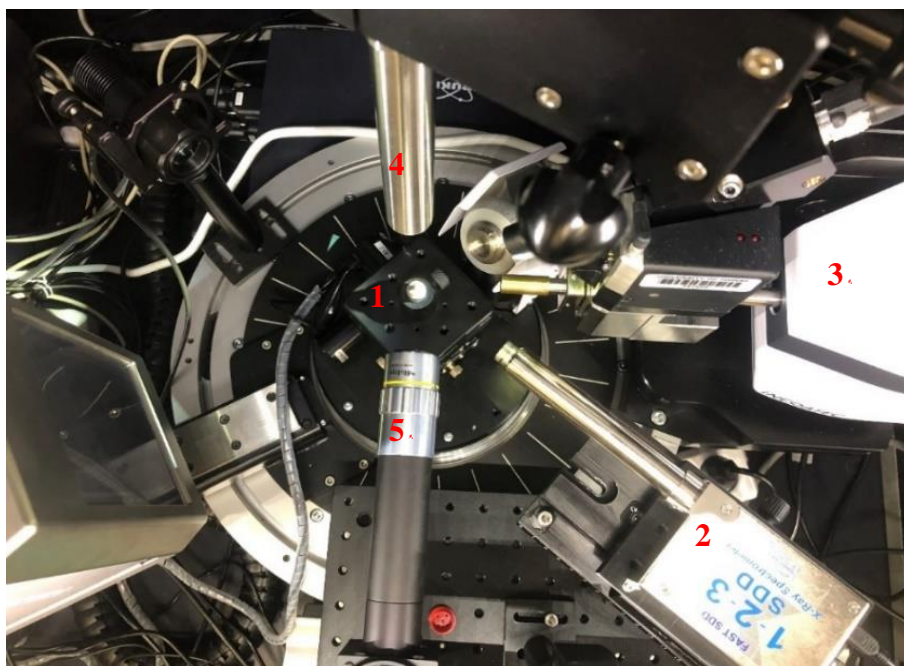
Figure 4. Top view of the D8 Venture instrument with micro-XRF platform. (1) Motorized sample XYZ stage, (2) Amptek XRF detector, (3) Ag K_α microfocus source, (4) Oxford Cryostream adapted to blow liquid nitrogen stream on the sample,(5) Objective of the XRF high resolution viewing system.
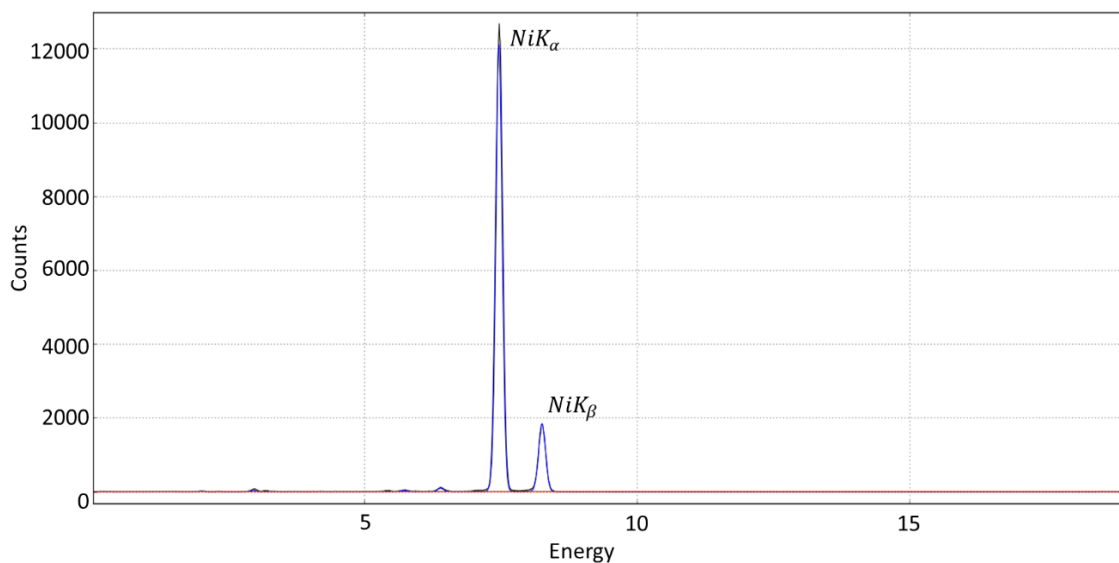
Figure 5. The XRF spectrum peak of Ni end-member schreibersite (Ni_3P). The two visible peaks correspond to NiK_α and NiK_β, the emission lines of the main metal element of this synthetic mineral.

2.2 X-ray Diffraction

X-ray diffraction is a technique for qualitative and quantitative analysis of minerals and other crystalline compounds. The diffraction pattern comes from the interference effect between X-rays and atoms inside the crystalline solid. In a typical diffractometer the X-rays are generated from the X-ray tube in order to produce a monochromatic incident beam. The interaction of the incident rays and the sample produces diffracted rays, in accordance with the conditions of Bragg's Law ($n\lambda = 2d \sin \theta$); where λ is the wavelength of the X-ray beam, n is an integer representing the order of the diffraction peak, 2θ is the scattering angle, and d is the interplanar distance between lattice planes of the crystal (Bragg & Bragg, 1913). The unique set of interplanar distances, referred to as d-spacing, along with corresponding diffraction peak intensities, allow us to identify and determine the crystal structure and unit cell parameter of minerals.

The X- ray diffraction experiments for this project were conducted using the single crystal X-ray diffraction technique. The synthetic single crystal was mounted on a Kapton loop and then

aligned with the center of the instrument using a goniometer head (Figure 6). The data collection was conducted using APEX3 software (Bruker, 2016). The atomic positions, bond lengths and angles can be identified and analyzed with the SHELXL program (Sheldrick, 2008a).
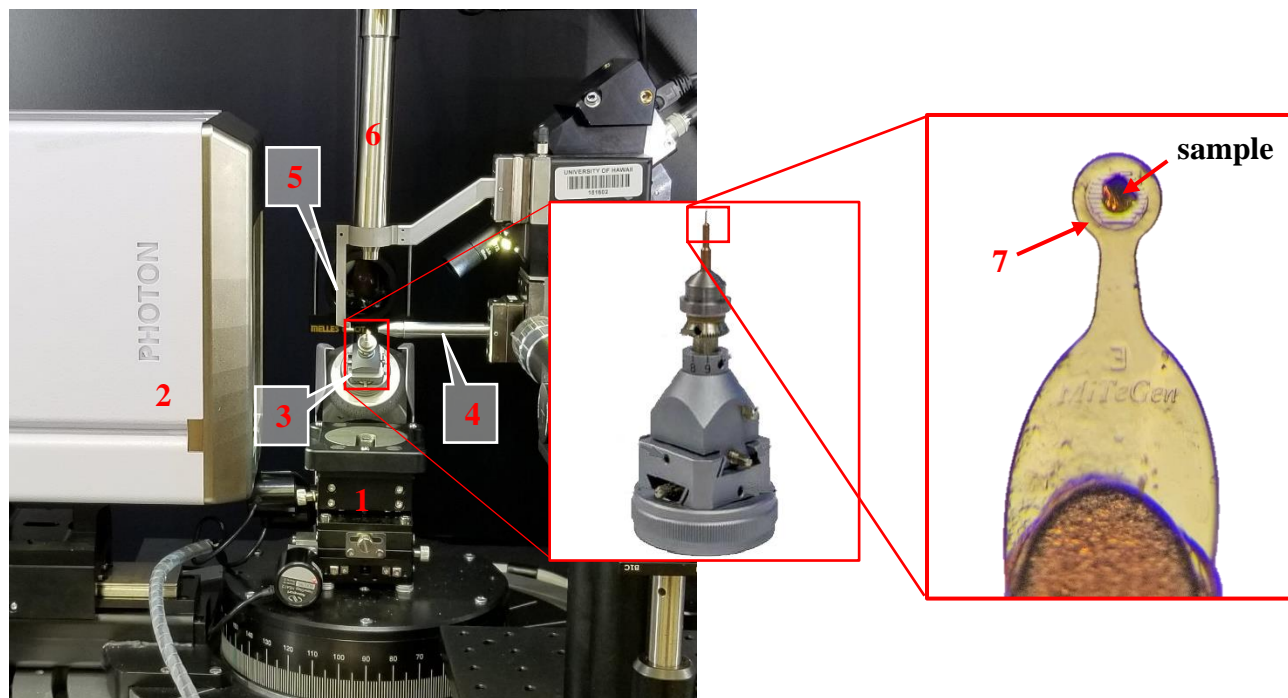
Figure 6. The single crystal X-ray diffraction components. (1) Motorized sample XYZ stage, (2) Photon detector, (3) Goniometer head, (4) Collimator, (5) Beam stop (6) Oxford Cryostream adapted to blow He stream on the sample, (7) Kapton loop.

2.3 High pressure experiments

Diamond anvil cell (DAC) is an instrument used for subjecting microscopic samples to high pressure conditions. DAC generates high pressure by applying a large force to a small area between two cutlet faces of two opposed anvil-shaped diamonds. A DAC consists of six main components: metallic cell body, backing plates (diamond seats), diamond anvils, a gasket, screws, and Belleville washers, as shown in Figure 7. The proper preparation of the DAC is very important for the success of the experiment. The preparation begins with mounting the diamond on a diamond seat, aligning the center of the diamond culets with the center of the seat, and then gluing the

10

diamond with black Stycast® epoxy. The next step is placing the two glued diamonds in DAC and securing with screws. For this step, we have to ensure that the two diamond cutlets are parallel, and their centers are colinear. After that, the metal gasket is placed between the two diamond cutlets for pre-indentation. Before indentation, the washers should be specifically stacked for each of the diamond cell screws because they are designed to recoil and store energy and thus provide a smooth increase of force. After the screws and carefully arranged washers are inserted into the DAC, one can slowly turn the screws to indent the metal gasket to obtain a thickness around 0.040 mm. Gasket thickness during pre-indentation can be estimated by measuring the distance between the top and bottom parts of the DAC with a micrometer. Once the pre-indentation is complete, the gasket is removed from the DAC and laser drilling is used to create a circular hole at the center of the indentation. The diameter of the hole depends on the size of diamond cutlets and type of pressure transmitting medium to be used. The components of the DAC used in our experiments are shown in Figure 7.
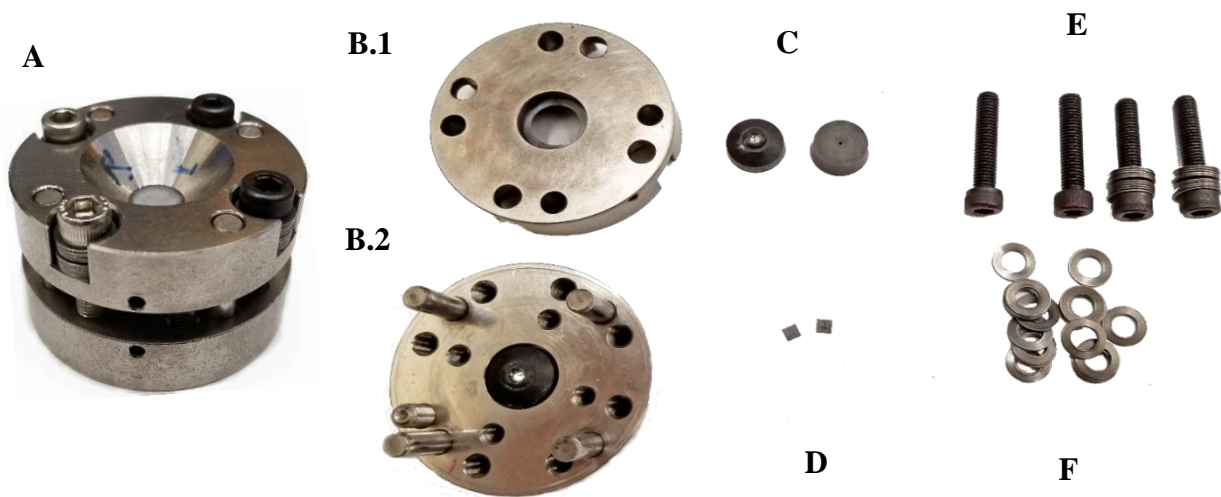
Figure 7. The components of the DAC used in our experiments. (A) The assembled diamond anvil cell (DAC) which consists of (B.1 and B.2) metallic DAC frame, (C) backing plates (diamond seats), (D) gasket, (E) screws, and (F) Belleville washers.

A DAC is a uniaxial compression device, however, the best quality in situ X-ray diffraction experiments require hydrostatic conditions (equal stress acting on the sample from all directions). To transmit pressure to the sample in a close-to hydrostatic manner, the gasket hole, is filled with a soft pressure transmitting medium surrounding the studied sample. Common quasi-hydrostatic media include noble gases He, Ne, Ar, N_2, ambient liquids (methanol ethanol mixture, silicone oil, fluorinert), or soft solids (e.g., NaCl) (Rivers et al., 2008; Klotz et al., 2009). In order to determine the pressure inside the DAC sample chamber, the majority of DAC studies use the ruby fluorescence technique (Mao et al., 1978, 1986). Ruby crystals $(Al_{0.03}Cr_{0.97})_2O_3$, when irradiated with intense light (typically green laser), emit fluorescent light in the red part of the spectrum (two strong peaks referred to as R1 and R2, shown in Figure 8). The position of this emission shifts to higher wavelengths at high pressure. Several existing calibration scales allow one to calculate pressure from the R1 line wavelength (e.g., Mao et al., 1986; Dewaele et al., 2008). In all of our experiments, the wavelength shift of ruby fluorescence was used to determine pressure based on the equation $(\Delta\lambda/\lambda_0)$ with $P (GPa) = A/B\{[1 + (\Delta\lambda/\lambda_0)]^B - 1\}$, where A is fixed at 1904 GPa, B = 5 for the non-hydrostatic scale (Mao et al., 1978) and 7.665 for the quasi-hydrostatic scale (Mao et al., 1986), λ_0 is the wavelength measured at 1 bar, $\Delta\lambda$ is the wavelength shift from the value observed at 1 bar to the value observed at pressure P (e.g., Mao et al., 1978, 1986; Silvera et al., 2007; Jacobsen et al., 2008).
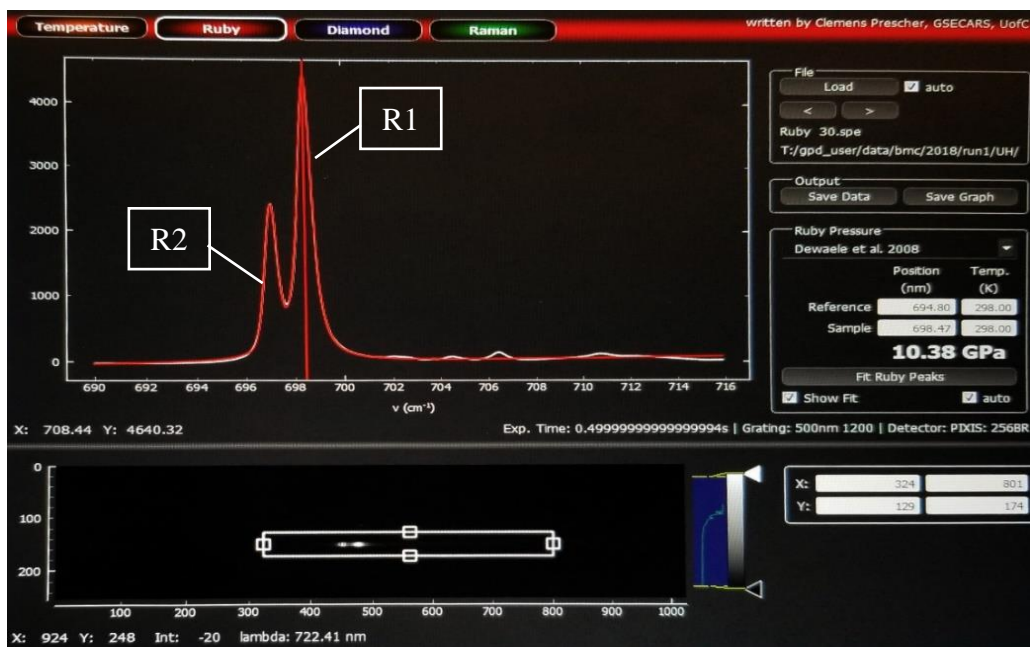
Figure 8. The intensity of ruby fluorescence peak. Ruby fluorescence spectrum showing R1 and R2 peaks from T-Rax program.

One of the limitations of the ruby pressure scale is that when the sample is heated, the fluorescence peak broadens and decreases in intensity. Another method used for determination of pressure inside DAC, particularly useful in high temperature experiments, is to load a secondary diffraction-based pressure calibrant inside the sample chamber, typically a small piece of gold or platinum foil (Heinz & Jeanloz, 1984; Dorfman et al., 2012; Ye et al., 2017). In this case, pressure inside the sample chamber can be calculated from the equation of state of the secondary standard (Dorfman et al., 2012). The d-spacings of the diffraction peaks will change when pressure and temperature change. The thermal equation of state can be used to calculate pressure and temperature from the d-spacings.

In this project, we used the DAC technique to investigate compressional behavior of Ni_3P at ambient temperature. Experiment 1 used synchrotron powder X-ray diffraction. Finely ground powder of synthetic Ni_3P was loaded into the diamond anvil cell with 0.300 mm culet-size standard

13

diamonds mounted on asymmetric backing plates (cubic boron nitride towards the X-ray source and tungsten carbide towards the detector). A piece of Re metal foil with initial thickness of 0.255 mm was pre-indented to 0.039 mm. The sample chamber was made by drilling a hole with 0.180 mm diameter in the pre-indented gasket using laser cutting. A piece of gold foil and a ruby sphere were placed in the sample chamber, next to the sample for the pressure calibration (Heinz & Jeanloz, 1984; Mao et al., 1978, 1986). The diamond anvil cell (DAC) was loaded with neon to ~0.5 GPa as the pressure medium using the GSECARS/COMPRES gas loading system (Rivers et al., 2008). Microphotograph of the sample is shown in Figure 9.
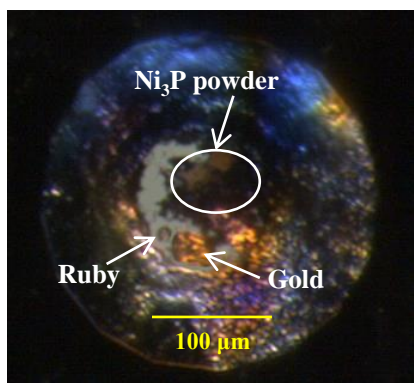
Figure 9. The powder sample of Ni_3P inside the DAC after loading neon as the pressure medium.

The X-ray diffraction experiment was conducted at experimental station 13-BM-C, Advanced Photon Source (APS), Argonne National Laboratory and a monochromatic incident beam with wavelength of 0.434 Å (28.6 keV) was used (Figure 10). The incident beam was focused by a pair of Kirkpatrick-Baez mirrors to a focal spot of approximately 0.015 by 0.015 mm. A MAR165 charge-coupled device (CCD) detector for recording the diffraction images was placed approximately 180 mm from the sample. Lanthanum hexaboride (LaB_6) powder was used to calibrate the distance and the tilting of the detector. The total angular opening of DAC was ± 12°. The sample was kept motionless during the exposure, with typical exposure time of 5 seconds. The

data were integrated and converted to 1-dimmensional diffraction patterns using the Dioptas program (Prescher & Prakapenka, 2015).
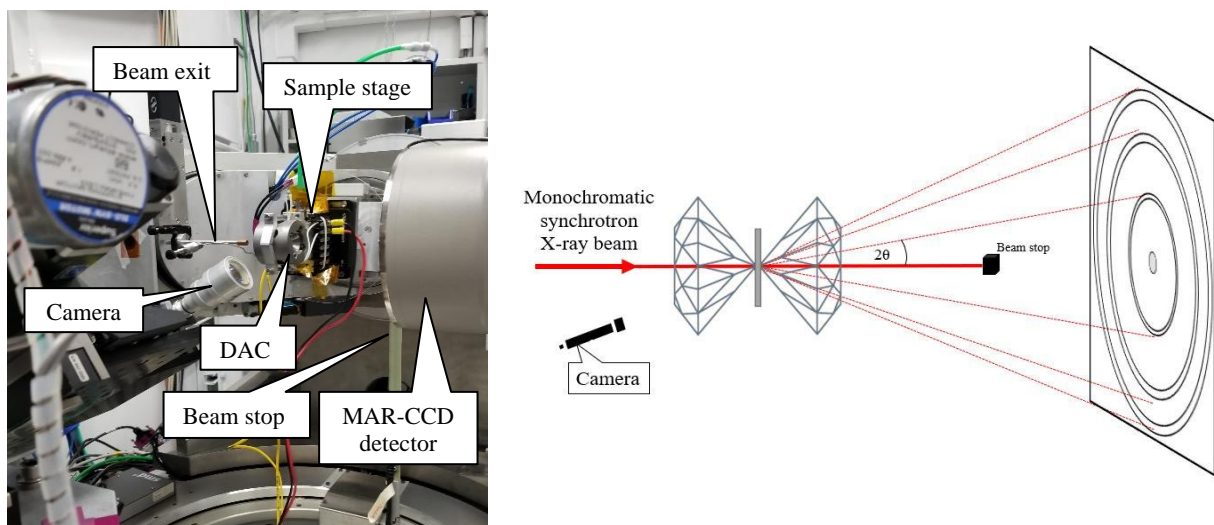
Figure 10. (A) The synchrotron x-ray diffraction instrument at station 13-BM-C, Advanced Photon Source (APS). The pinhole (beam exit) is in the left, diamond anvil cell (DAC) (mounted on sample stage) in the middle, the detector is in the right, and the beam stop is in between the DAC and the detector. (B) Simple sketch of synchrotron x-ray diffraction when the X-ray beam passes through the diamonds and diffracts from the sample to the detector.

Experiment 2 employed the synchrotron single crystal X-ray diffraction technique. Two synthetic single crystals of Ni_3P, C1 and C2, with approximate sizes of $0.040 \times 0.025 \times 0.005$ mm and $0.020 \times 0.020 \times 0.005$ mm respectively were loaded into the DAC with standard diamonds (0.300 mm cutlets) and were mounted on asymmetric backing plates (cubic boron nitride towards the X-ray source and tungsten carbide towards the detector). Crystal C1 was mounted with (001) direction perpendicular to the diamond's cutlet and C2 was mounted with the (001) parallel to the cutlet, as shown in Figure 11. The Re metal foil with initial thickness at 0.255 mm was pre-indented to 0.045 mm. The sample chamber was prepared by drilling a hole with 0.180 mm diameter in the pre-indented gasket using laser cutting. Gold and two ruby spheres were placed in the sample chamber, next to the samples for pressure calibration (Mao et al., 1986). The DAC was loaded to

~0.5 GPa with neon as the pressure medium using the GSECARS/COMPRES gas loading system (Rivers et al., 2008).
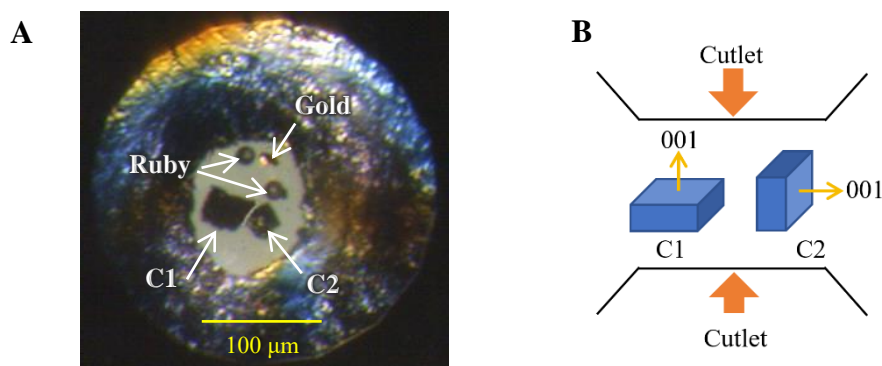
Figure 11. The single crystal samples of Ni_3P inside the DAC after loading neon as the pressure medium. (A) The single crystal samples of Ni_3P after loading neon as the pressure medium. C1 is the crystal mounted with (001) direction perpendicular to the diamond's cutlet. C2 is the crystal mounted with (001) direction parallel to the diamond's cutlet. (B) The model shows the DAC loading force directional relationship with the samples.

The characteristics of the beam and the instrument in experiment 2 were the same as in experiment 1 (Figure 10). The total angular range covered during the scans was from $\varphi = 57$ to $123°$ (total angular opening of $\pm 33°$). A series of step and wide-step φ-exposures were collected. Step scans involved $1°$ angular increments, and wide-step scans had $9.8°$ angular increments. The sample was rotated at constant speed during the exposure, with typical exposure time of 1s/deg. The single crystal X-ray diffraction data were analyzed with GSE_ADA and Reciprocal Space Viewer (RSV), as described by Dera et al. (2013). Refinement of the crystal structure was done with the program SHELXL (Sheldrick, 2008a).

2.4 Data analysis

The first step to analyze the powder diffraction data from an area detector like a CCD is to determine geometric parameters, such as the sample to detector distance and detector tilts, using a diffraction standard for which the d-spacings are well known. In our powder experiments we used

LaB$_6$ as the calibrant and performed calibration refinement using the Dioptas program. The refined

detector parameters can be stored as .poni files using either pyFAI geometry parameters (Ashiotis,

et al., 2015) or using equivalent calibration parameters defined in fit2D geometry (Hammersley,

1997). In the integration window in the Dioptas program, the diffraction data from the experiment

are displayed in the left window, while the corresponding integrated diffraction pattern is shown

in the right window as a white curve (Figure 12). The green circle in the diffraction image

corresponds to the position of the green vertical line in the diffraction pattern. The yellow and blue

lines represent the reference diffraction pattern from the Joint Committee on Powder Diffraction

Standards (JCPDS) database. Collected XRD spectra can be conveniently compared with the

database reference spectra to identify and index different phases present in the sample.
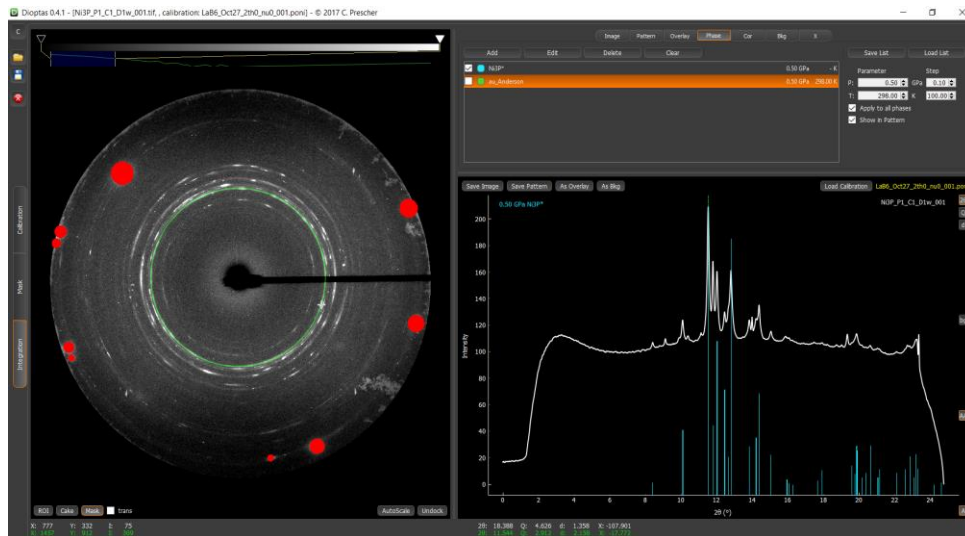
Figure 12. Screenshot of the Dioptas program. The powder diffraction data from the experiment
are displayed in the left panel and the corresponding diffraction pattern in shown in the right panel
as a white curve. The red circles were masked for removing the diffraction peaks of the diamond.

For the single crystal experiment, the calibration data recorded for LaB$_6$ powder sample

can be stored as .cal files in GSE_ADA program (Dera et al., 2013). Peak fitting and peak intensity

correction for DAC absorption, Lorenz and polarization effects and sample displacement effects

17

were performed in GSE_ADA. The effects of sample absorption were ignored due to the high incident energy, low absorption coefficient and negligible sample thickness. The RSV program allows access to two external programs: XPREP (Sheldrick, 2008b) for selecting the conventional symmetry setting and space group determination, and CELL_NOW (Sheldrick, 2003) for peak indexing, unit cell parameter determination, and the orientation matrix. The crystal structure model was refined using the least-squares method with anisotropic atomic displacement parameters for all atoms in SHELXL (Sheldrick, 2008a).

The Equation of State (EoS) is used for describing the response of a volume of material to changes in physical conditions. The EOS is a function of thermodynamic parameters such as temperature (T), pressure (P), and volume (V). In this project an isothermal EOS was used to describe the relationship between the unit cell volume and pressure. Typically, an EOS uses bulk modulus or incompressibility ($K = -V (\partial P/\partial V)$) where K is the bulk modulus, and $\partial P/\partial V$ is the partial derivative of pressure with respect to volume. The bulk modulus describes the resistance of material to changes in volume under compression. All materials become more incompressible at higher pressure, which is reflected in increasing bulk modulus. The equation of a linearly increasing K can be written as $K = K_{T0} + K'*P$, where K_{T0} is the bulk modulus at room pressure and $K' = (\partial K/\partial P)_{P=0}$ is the pressure derivative of K. In order to find a relationship between the volume of the crystal and pressure, the Birch–Murnaghan isothermal equation of state (BM-EoS) was used. The third order Birch–Murnaghan equation of state has the following form:

$$P(V) = \frac{3K_0}{2} \left[\left(\frac{V_0}{V}\right)^{\frac{7}{3}} - \left(\frac{V_0}{V}\right)^{\frac{5}{3}} \right] \left\{ 1 + \frac{3}{4}(K'_0 - 4)\left[\left(\frac{V_0}{V}\right)^{\frac{2}{3}} - 1 \right] \right\},$$

where P is pressure, V is the deformed volume, V_0 is the reference volume, K_{T0} is the bulk modulus, and K'_0 is the derivative of the bulk modulus with respect to pressure (Birch, 1947; Murnaghan, 1937, 1944).

18

3. Experimental results

3.1 Single crystal X-ray diffraction at ambient conditions

Results of the single crystal X-ray diffraction experiment at ambient pressure show that unit cell parameters of the Ni end-member schreibersite (Ni_3P) are $a = 8.9515(2)$ Å, $c = 4.3859(1)$ Å, and $V_0 = 351.44(8)$ Å^3 at ambient conditions, consistent with the tetragonal structure with $I\bar{4}$ space group. The fractional atomic coordinates and interatomic distances (bonding distance) in Ni_3P at ambient pressure are summarized in Tables 3 and 4, respectively. The basic principle of least squares structure refinement is based on the Fourier transformation from the model coordinates and atomic scattering factors. The simple formula for the refinement figure of merit is $R1 = \Sigma\, ||F_o| - |F_c||\, /\, \Sigma\, |F_o|$ where F_o represents experimentally measured structure factor amplitudes, and F_c represents structure factor amplitudes calculated from the current model. R1 would ideally be zero if no differences between the measured and calculated peak intensities exist. Structure refinement is usually considered satisfactory if R1<0.1. The final R1-value obtained in our experiment was 0.0239. The structure of Ni_3P determined in this experiment is shown in Figure 13.

Table 3. Fractional atomic coordinates of Ni_3P at ambient pressure and temperature (Numbers in parentheses represent errors in the last digit).

Element	x	y	z
Ni	0.9228(1)	0.8887(1)	0.7608(1)
Ni	0.6353(1)	0.9675(1)	0.0219(1)
Ni	0.8313(1)	0.7802(1)	0.2458(1)
P	0.7139(1)	0.9517(1)	0.5192(2)

Table 4. Bonding interatomic distances in Ni$_3$P at ambient pressure and temperature (Numbers in parentheses represent errors in the last digit).

	Interatomic distance (Å)
Ni$_I$ - Ni$_I$	2.425(1), 2.710(1)x2, 2.859(1)
Ni$_I$ - Ni$_{II}$	2.649(1)
Ni$_I$ - Ni$_{III}$	2.478(1), 2.592(1), 2.708(1), 2.732(1), 2.813(1)
Ni$_{II}$ - Ni$_{II}$	2.491(1), 2.669(1), 2.669(1)
Ni$_{II}$ - Ni$_{III}$	2.511(1), 2.544(1), 2.618(1)
Ni$_{III}$ - Ni$_{III}$	2.687(1), 2.687(1)
Ni$_I$ - P	2.222(1), 2.284(1)
Ni$_{II}$ - P	2.296(1), 2.317(1), 2.318(1), 2.345(1)
Ni$_{III}$ - P	2.214(1), 2.278(1), 2.337 (1)
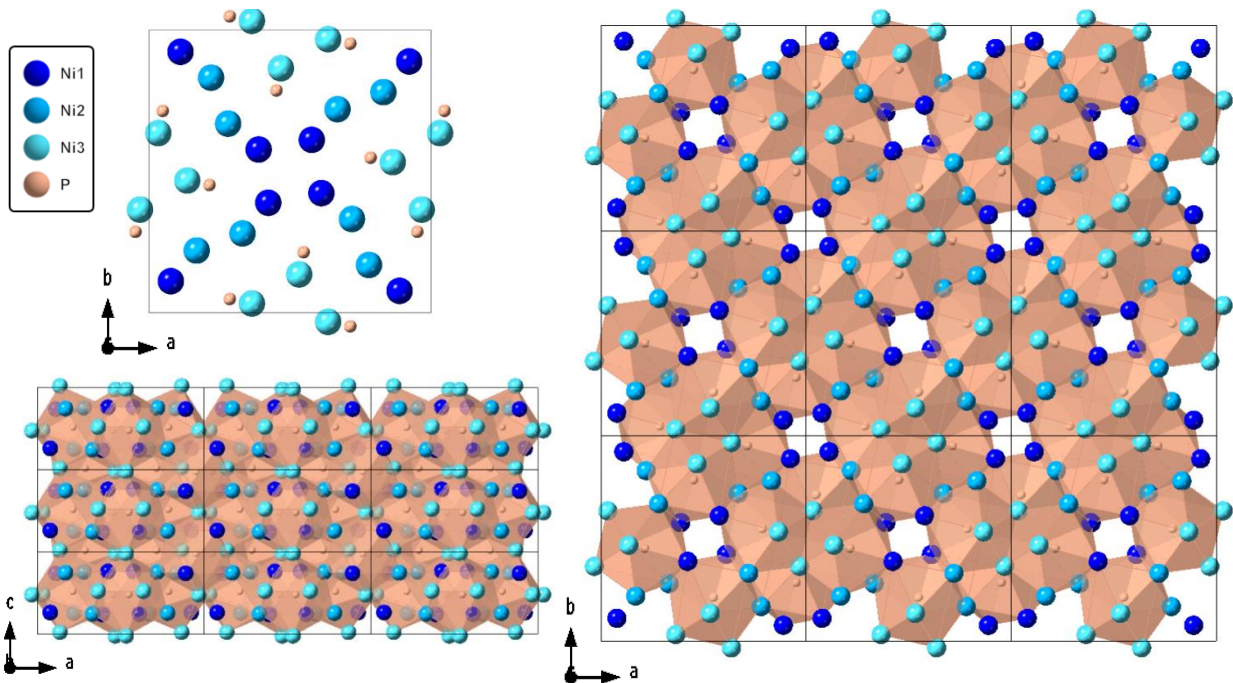
Figure 13. The crystal structure of Ni$_3$P at ambient pressure and temperature.

3.2 Diffraction pattern and unit cell parameter evolution to 50 GPa

The powder experiment was conducted in the pressure range of 0.5−46.0 GPa at ambient temperature. The integrated data were plotted as diffraction intensity against scattering angle 2θ. The unit cell parameters can be calculated from the Bragg's Law using the d-spacing formula for

a tetragonal system ($\frac{1}{d^2} = \frac{h^2+k^2}{a^2} + \frac{l^2}{c^2}$) where h, k, l represent the Miller indices and a and c represent unit cell parameters. The unit cell parameters obtained from the powder data at the first pressure point were $a = 8.945(1)$ Å, and $c = 4.381(1)$ Å, consistent with a tetragonal structure. The crystal structure remains tetragonal on compression to 46.0 GPa (Table 5). The ratio of the unit cell parameters (c/a) as a function of pressure remains constant with a little scatter around 0.4897(1) below 35.0 GPa. Above 35.0 GPa, the c/a ratio increases significantly and approaches 0.492(1) at 46.0 GPa (Figure 14). The normalized lattice parameters (a/a_0 and c/c_0) show a decrease at a continuous rate for both parameters until 46 GPa, whereas, the slope of c changes discontinuously at 35 GPa (Figure 15). This led to a change of the c/a ratio.

The single crystal experiment was conducted over pressure range 1.1−49.5 GPa at ambient temperature. Because of the different orientation of the two sample crystals, the corresponding diffraction patterns were different, as shown in Figure 16. The unit cell parameter of the two samples are shown in Table 6. The unit cell parameters at 1.1 GPa confirm that both single crystals are tetragonal, with $a = 8.939(1)$ Å, and $c = 4.378(2)$ Å for C1 and $a = 8.936(1)$ Å, $c = 4.375(1)$ Å for C2. Similar to the powder experiment, the trend of the c/a ratio is constant at around 0.4899(3) below 30.0 GPa, and starts increasing significantly above that pressure, approaching 0.4928(4) at 49.5 GPa. For crystal C2, although the ratio of the cell parameter c/a is constant at around 0.4897(2) below 24.95 GPa, it starts to increase substantially above that pressure and reaches 0.4931(6) at 49.5 GPa, as shown in Figure 14. Moreover, between 40 GPa and 45 GPa, both single crystals exhibited little change in the c/a ratio and remained approximately constant close to 0.4924(4). The normalized lattice parameters (a/a_0 and c/c_0) for the single crystal experiment revealed that there is a slight decrease of slope in the c-axis at 30 GPa for C1 and 25 GPa for C2, which contributed to the change of c/a ratio from both crystals, as shown in Figure 15.

21
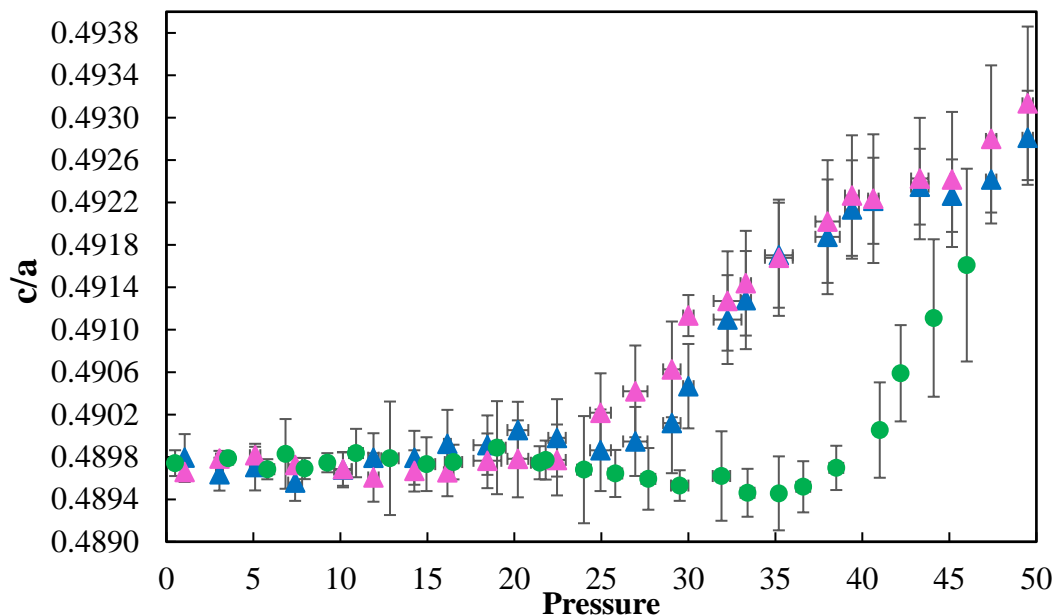
Figure 14. The *c/a* axial ratio of Ni$_3$P at different pressures. Green circles show the data from powder diffraction experiment, and the blue and purple triangles represent data from single crystal 1 and single crystal 2, respectively. All experiments were conducted at room temperature.
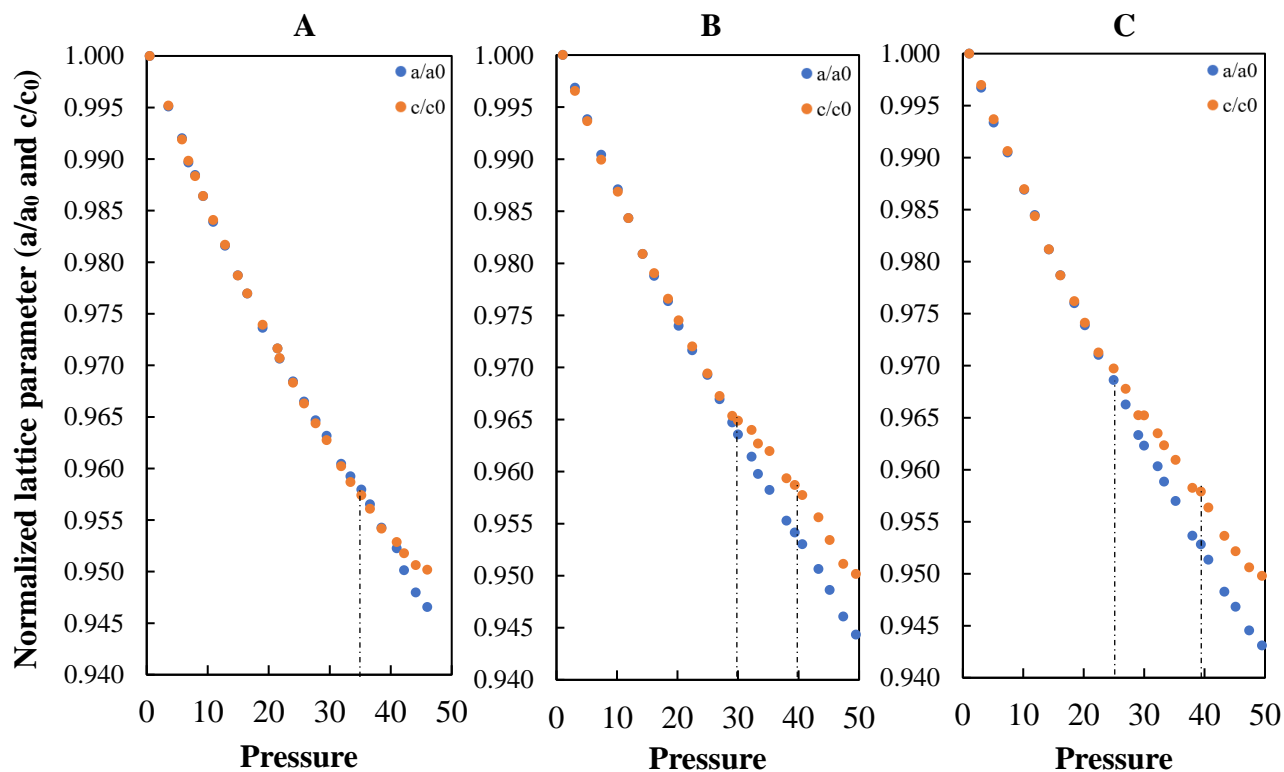
Figure 15. The normalized lattice parameters (*a/a$_0$* and *c/c$_0$*) of Ni$_3$P from this study. (A) Powder data, (B) Single crystal 1, and (C) Single crystal 2. The blue dots represent the normalized lattice parameter *a*, and the orange dots represent the normalized lattice parameter *c*.

22
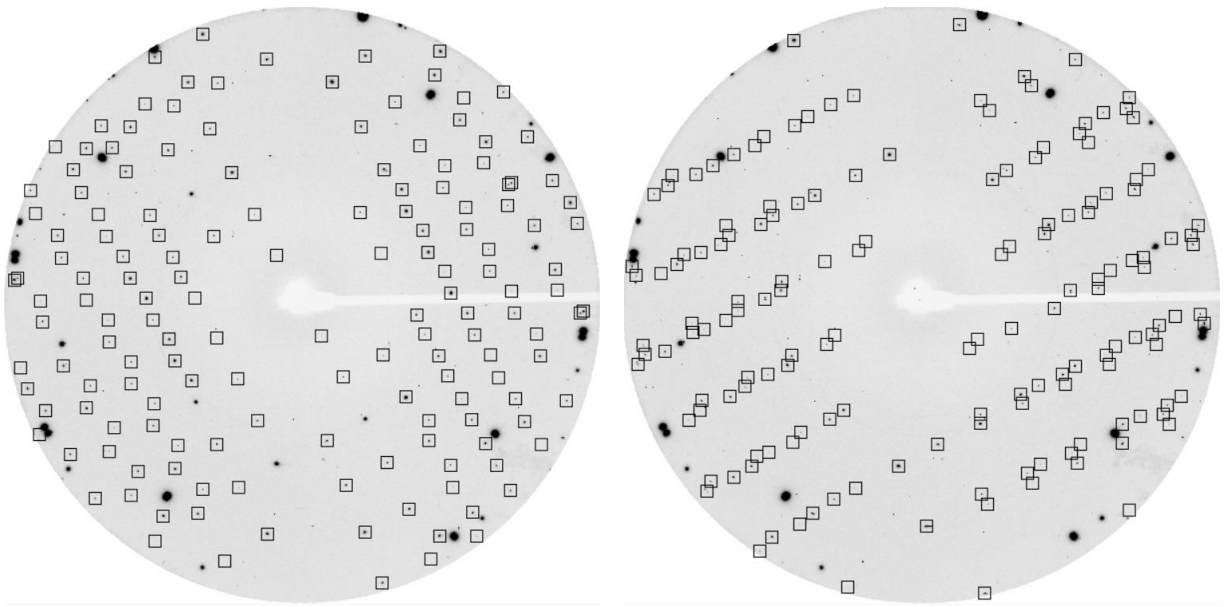
Figure 16. The single crystal X-ray diffraction patterns of Ni$_3$P. (A) Diffraction pattern from Crystal C1, mounted with (001) direction perpendicular to the cutlet. (B) Diffraction pattern from C2, mounted with the (001) parallel to the cutlet. Black squares mark locations of observed peaks position. The strong reflections are from the diamond anvils.

Table 5. Pressure dependence of unit cell parameters of Ni$_3$P determined in the powder diffraction experiment (Numbers in parentheses represent errors in the last digit).

Pressure (GPa)	a [Å]	c[Å]	Volume [A^3]
0.50(1)	8.945(1)	4.381(1)	350.5(1)
3.6(2)	8.901(1)	4.360(1)	345.5(1)
5.8(4)	8.874(1)	4.345(1)	342.2(1)
6.9(3)	8.853(4)	4.336(2)	339.9(4)
8.0(3)	8.842(1)	4.330(1)	338.5(1)
9.3(3)	8.824(1)	4.321(1)	336.5(1)
10.9 (4)	8.801(2)	4.311(2)	334.0(2)
12.9(5)	8.781(4)	4.301(4)	331.6(5)
15.0(5)	8.755(2)	4.288(2)	328.6(3)
16.5(5)	8.739(2)	4.280(1)	326.9(2)
19.0(5)	8.709(4)	4.267(3)	323.6(4)
21.5(5)	8.692(1)	4.257(1)	321.6(2)
21.8(1)	8.683(2)	4.253(1)	320.6(2)
24.0(4)	8.663(6)	4.242(3)	318.4(6)
25.8(4)	8.646(2)	4.233(2)	316.4(2)
27.7(4)	8.629(3)	4.225(2)	314.6(3)
29.5(5)	8.616(2)	4.218(1)	313.1(2)
31.9(5)	8.592(4)	4.207(3)	310.5(4)
33.4(4)	8.581(3)	4.200(1)	309.4(3)
35.2(3)	8.569(4)	4.194(2)	308.0(4)
36.6(4)	8.556(2)	4.189(2)	306.7(2)
38.5(4)	8.536(3)	4.180(1)	304.6(3)
41.0(2)	8.518(4)	4.174(3)	302.9(4)
42.2(2)	8.499(5)	4.170(3)	301.2(5)
44.1(1)	8.480(7)	4.165(5)	299.5(7)
46.0(2)	8.467(7)	4.163(7)	298.4(8)

Table 6. Pressure dependence of unit cell parameters of Ni_3P determined in single crystal diffraction experiment (Numbers in parentheses represent errors in the last digit).

Pressure (GPa)	Crystal	a [Å]	c[Å]	Volume [A^3]
1.1(1)	C1	8.939(1)	4.378(2)	349.8(2)
	C2	8.936(1)	4.375(1)	349.4(1)
3.1(2)	C1	8.911(1)	4.363(1)	346.4(1)
	C2	8.906(1)	4.362(1)	346.0(1)
5.1(3)	C1	8.883(1)	4.350(2)	343.3(2)
	C2	8.876(1)	4.348(1)	342.6(1)
7.4(4)	C1	8.853(1)	4.334(2)	339.7(1)
	C2	8.851(1)	4.334(1)	339.5(1)
10.2(5)	C1	8.823(1)	4.321(1)	336.4(1)
	C2	8.819(1)	4.318(1)	335.8(1)
11.9(3)	C1	8.799(1)	4.309(2)	333.6(2)
	C2	8.797(1)	4.307(2)	333.3(2)
14.3(1)	C1	8.768(1)	4.294(2)	330.1(2)
	C2	8.767(1)	4.293(2)	330.0(1)
16.2(2)	C1	8.749(1)	4.286(3)	328.1(2)
	C2	8.745(1)	4.282(2)	327.5(2)
18.5(8)	C1	8.727(1)	4.276(2)	325.7(2)
	C2	8.721(1)	4.271(2)	324.9(2)
20.2(6)	C1	8.706(1)	4.266(2)	323.4(2)
	C2	8.702(1)	4.262(3)	322.8(2)
22.5(5)	C1	8.685(1)	4.256(3)	321.0(2)
	C2	8.677(1)	4.250(3)	319.9(2)
25.0(6)	C1	8.664(1)	4.244(3)	318.6(3)
	C2	8.655(1)	4.243(3)	317.8(3)
27.0(7)	C1	8.643(1)	4.235(3)	316.3(2)
	C2	8.634(2)	4.234(4)	315.7(3)
29.1(5)	C1	8.623(1)	4.226(4)	314.3(3)
	C2	8.608(2)	4.223(4)	312.9(3)
30.0(3)	C1	8.613(1)	4.224(3)	313.4(3)
	C2	8.599(2)	4.223(1)	311.0(1)
32.3(8)	C1	8.594(1)	4.220(4)	311.7(3)
	C2	8.581(2)	4.216(4)	310.4(3)
33.3(3)	C1	8.579(1)	4.215(4)	310.2(3)
	C2	8.568(2)	4.211(4)	309.1(3)
35.2(8)	C1	8.565(1)	4.212(4)	309.0(3)
	C2	8.551(2)	4.204(5)	307.5(3)
38.0(7)	C1	8.539(2)	4.200(5)	306.2(3)
	C2	8.521(2)	4.193(5)	304.5(4)
39.4(4)	C1	8.529(1)	4.197(4)	305.3(3)
	C2	8.514(2)	4.191(5)	303.8(4)
40.6(3)	C1	8.519(1)	4.193(3)	304.3(3)
	C2	8.501(2)	4.184(5)	302.4(4)
43.3(5)	C1	8.497(1)	4.184(3)	302.1(2)
	C2	8.473(2)	4.173(5)	299.6(4)
45.2(1)	C1	8.479(1)	4.174(3)	300.1(2)
	C2	8.460(2)	4.166(5)	298.2(4)
47.4(3)	C1	8.457(1)	4.164(3)	297.8(3)
	C2	8.440(2)	4.159(6)	296.3(4)
49.5(3)	C1	8.441(1)	4.160(4)	296.4(3)
	C2	8.427(3)	4.156(6)	295.1(4)

3.3 Volumetric compressibility, equation of state, and bulk modulus

The volume and pressure data from all experiment in this project were used to fit the 3rd order Birch–Murnaghan equation of state (BM-EoS) with the EOS-FIT7 program (Gonzalez-Platas et al., 2016). Based on the volume independently constrained at ambient conditions ($V_0 = 351.44(8)$ $Å^3$), the BM-EoS fit of powder data below 35 GPa yielded a bulk modulus of $K_{T0} = 190(4)$ GPa, and its pressure derivative $K' = 4.9(4)$. A discontinuity in compressibility is observed over 35 GPa. For the single crystal experiment, the BM-EoS fit of C1 data below 30 GPa yielded the values $K_{T0} = 199(5)$ GPa, $K'=4.7(4)$. Similarly, the volume of C2 data below 25 GPa of Ni_3P also fitted by 3rd BM-EoS, yielded the values $K_{T0} = 194(5)$ GPa, $K'=4.7(8)$. The results of the BM-EoS fits are plotted in Figure 17.
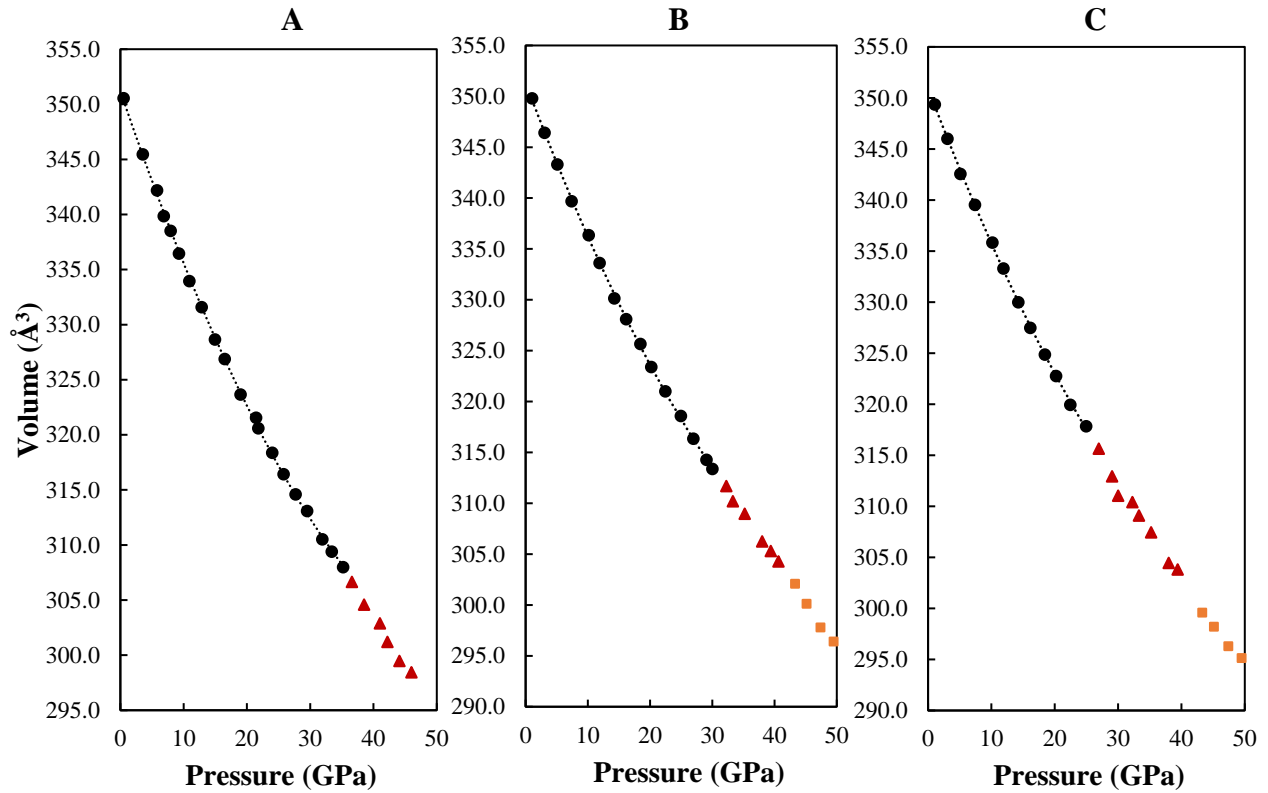
Figure 17. The volume-pressure curve of Ni_3P from high-pressure syn-XRD experiments. The black circle of Powder data below 35 GPa (A), C1 data below 30 GPa (B) and C2data below 25 GPa (C) were fitted by 3rd order Birch–Murnaghan equation of state. The red triangle represents the data after the first discontinuity. The orange square represents the data at second discontinuity.

The changes in bulk modulus as a function of pressure can be represented in a form of normalized pressure ($F = P[3f(1+2f)^{5/2}]^{-1}$) versus Eulerian strain ($f = 0.5[(V_0/V)^{2/3} -1]$) plot (Birch, 1978). *F-f* plot from all data indicates $K' > 4$ (Figure 18). The linear character of all three *F-f* plots indicates that the second pressure derivative of the bulk modulus (K'') is negligible.

Figure 18. The normalized pressure (GPa) vs Eulerian strain of Ni_3P. (A) Powder data, (B) Single crystal C1, and (C) Single crystal C2.

EoS fit confidence ellipses are used for visual quality assessment of the correlation between K_{T0} and K'. The confidence ellipses from all our data on Ni_3P are shown in Figure 19, drawn at

95.4% confidence level (2σ), indicating that all calculated K_{T0} and K' values from this study are consistent.
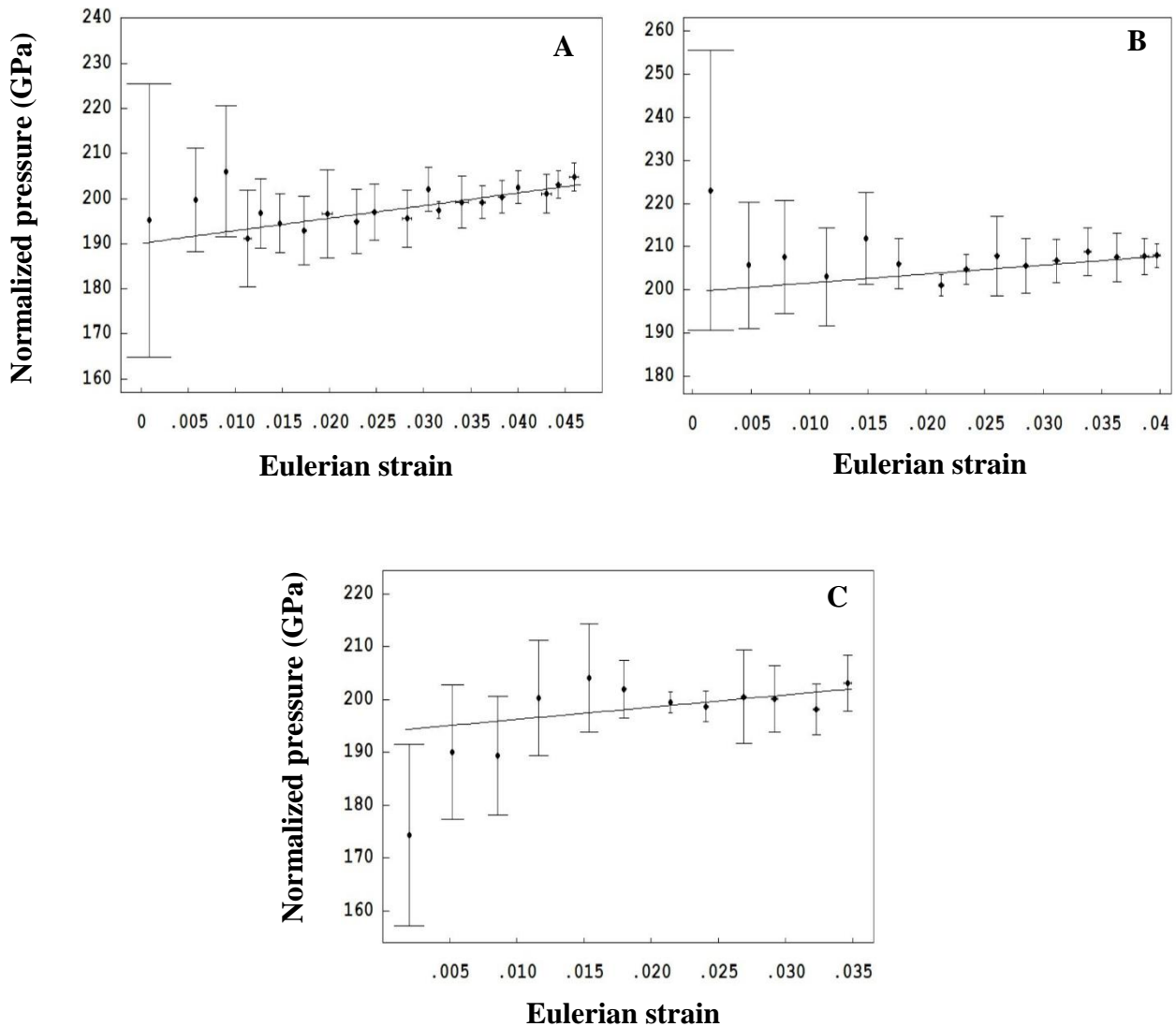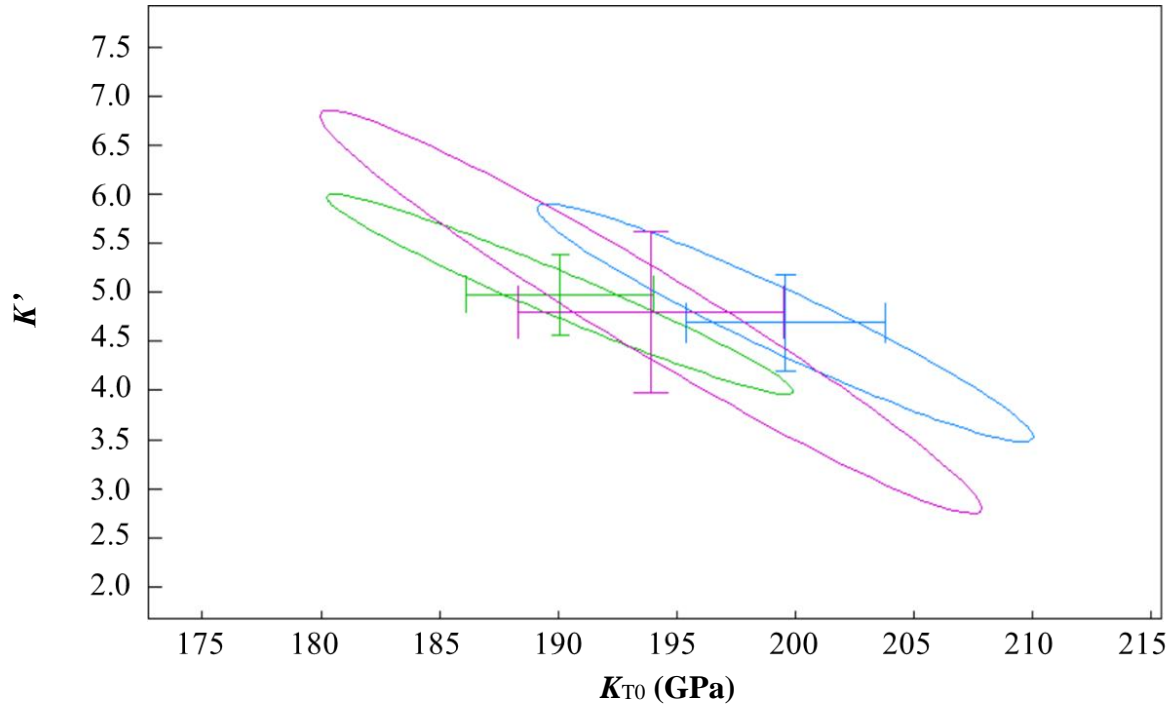

Figure 19. Confidence ellipses for the 3rd BM-EoS fits at 95.4% confidence (2σ). The green colored ellipse gives the data from powder sample, the blue colored ellipse gives the data from single crystal 1, and the purple colored ellipse gives the data from single crystal 2. The error bar corresponds to 1 e.s.d. on each of the individual parameters.

4. Discussion

4.1 Crystal structure at ambient condition.

The ambient unit cell parameters and interatomic distances of Ni_3P determined in this study are in very good agreement with previous reports (Aronsson, 1955; Rundqvist et al., 1962; Jun et al., 2007). The atomic coordinates of Ni_3P determined in our single crystal experiment represent the opposite absolute structure of the mineral, which is a well-known phenomenon for molecules or crystals without a center of symmetry or mirror plane. The space group of Ni_3P ($I\bar{4}$) does not include an inversion center (is acentric). The atomic coordinate data from this experiment are

inverted with respect to the coordinate data from previous studies (Aronsson, 1955; Rundqvist et al., 1962; Jun et al., 2007). However, despite this difference in absolute configuration, the structure of Ni_3P in this experiment is in excellent agreement with previously reported results.

4.2 Crystal structure evolution on compression to 50 GPa

At ambient conditions the unit cell axis and volume of Ni_3P is smaller than that of Fe_3P (Scott et al., 2007; Howard, 2010; Gu et al., 2014). This shows that the unit cell parameters are controlled mainly by the cation size, as the ionic radius of nickel (~1.24 Å) is smaller than that of iron (~1.26 Å).

The unit cell parameters of Ni_3P is approximately constant to 30 GPa, whereas for Fe_3P the constant behavior ends at 17 GPa. However, both Ni_3P and Fe_3P (Gu et al., 2014) show second subtle discontinuities in lattice parameter and in volume at approximately 40 GPa. The change in lattice parameters at 40 GPa might imply another electronic/magnetic transformation. Unfortunately, we are not able to verify the second transition convincingly due to the small number of pressure points collected above 40 GPa. The experimental results suggest that all of the axial compressibility of Ni_3P are almost identical up to the transition point, above which the c-axis becomes less compressible. Differences in the transition pressure observed in the three experiments (powder, C1 and C2) indicate that the stress state and the orientation of the uniaxial stress component have the effect of shifting the transition point. Gu et al. (2014), based on by first-principles calculations, reported magnetic collapse in Fe_3P around 40 GPa corresponding to a change of symmetry from $I\bar{4}$ to P4/mnc. The discontinuities of lattice parameter and volume as a function of pressure observed at approximately 30 GPa and 40 GPa in our experiments might be related to similar magnetic transitions. The change in the c/a ratio trend in Ni_3P in our study is very similar to the magnetic transition and analogous c/a change observed in Cr_2O_3 (Dera et al.,

2011b; Golosova et al., 2017). The decreasing compressibility in the c-axis, contributing to the discontinuity of the c/a ratio trend, suggests that there are different in magnetic structure at that transition point (Dera et al., 2011b).

The Bulk modulus (K_{T0}) of Ni_3P from this experiment is good agreement with the first-principle calculation result (Zhao et al., 2011). Moreover, the values of K_{T0} and K' of Ni_3P from our experiments are higher than were reported for the isostructural compounds such as Fe_3P (Scott et al., 2007; Howard, 2010; Gu et al., 2014), Fe_3S (e.g., Fei et al., 2000; Lin et al., 2004; Seagle et al., 2006; Kamada et al., 2010), and Ni_3S (Urakawa, et al., 2011). This suggests that the compressibility is controlled mainly by the cation size. Interestingly, K_{T0} and K' of Fe_3P and Fe_3S have quite similar values within the uncertainty, whereas K_{T0} and K' of Ni_3P are higher than Ni_3S. Changing the anion has a small effect on the compressibility behavior between Fe_3P and Fe_3S, but an effect on the compressibility between Ni_3P and Ni_3S is stronger. The cause of the differentiate is that the synthetic nickel of Ni_3P in this research is a stoichiometric compound while that of Ni_3S is non-stoichiometric compound. Moreover, Ni_3S studies were conducted only up to about 10 GPa, whereas in this study we compressed the sample to approximately 50 GPa. If we focus only on the first 10 GPa of Ni_3P data, we also found that the trend of the c/a ratio of C1 slightly decreases. Thus, to investigate the effect of the anion size between Ni_3P and Ni_3S, one might have to compress both samples to pressures higher than 10 GPa. The compressibility of the c-axis of Ni_3P, compared with the a-axis in our experiments is in good agreement with the compression behavior of the unit cell axis of Ni_3S (Urakawa et al., 2011).

4.3 Implications for planetary cores

In order to assess the effect of presence of Ni-rich schreibersite in the Earth core we compared densities of pure iron, Fe_3P and Ni_3P at pressures corresponding to inner and outer core (Figure 20). It should be noted that these calculations were done with extrapolation of results far beyond the region of conditions covered in our experiments. The comparison shows that the density of Ni_3P from this experiment and Fe_3P from Gu et al. (2014) are approximately 5% lower than the pure Fe at core pressure and ambient temperature (Figure 20). The result suggests that the presence of a significant amount of nickel and the light elements such as phosphorus has the effect of lowering the density and is consistent with the observed core density deficit from seismic evidence (e.g. Birch, 1952; Allègre et al., 1995; Li & Fei, 2003). Although our experiments did not include study of effects of high temperature on unit cell parameter of Ni_3P, in the first very simplified approximation we can just compare the cold compressibility curves.
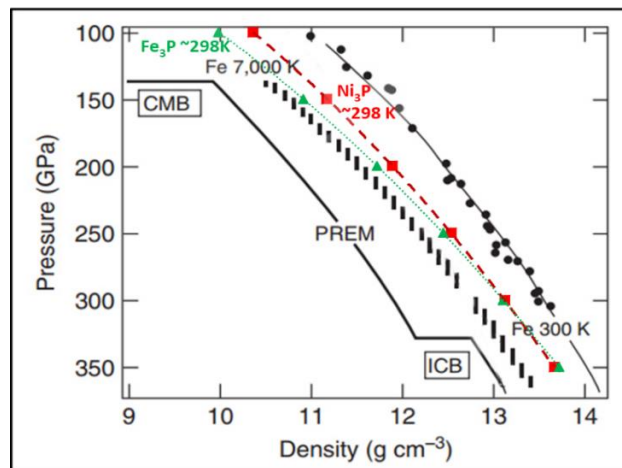
Figure 20. Comparison of the density of Ni_3P, Fe_3P, pure iron based on EoS and the density of the core from the Preliminary Reference Earth Model (PREM) (modified from Li & Fei, 2003). The red dash is the calculated density function of Ni_3P from this experiment. The green dots represent the calculated density function of Fe_3P (Gu et al., 2014). The solid line is the seismic data from PREM model (Dziewonski & Anderson, 1981). The solid circles are the measured densities of hcp-Fe from static experiments at 300K (Mao et al., 1990). The broken lines are calculated isothermal compression curve of hcp-Fe at 7,000K (Dubrovinsky et al., 2000).

Gu et al. (2014) reported that the discontinuities observed around 17 and 40 GPa were not only consistent with the calculated trend of magnetic transitions, but also resulted in discontinuous changes in thermal expansion parameter. The thermal expansion coefficient $\alpha(p)$ decreases with increasing pressure. By analogy, we can assume that the compressional discontinuities observed in our experiments for Ni_3P at approximately 30 GPa and 40 GPa might also be related to discontinuities of thermal expansion and magnetic transitions. Thermal expansion typically decreases with increasing pressure and with increasing bond energy, contributing to high melting point of materials at high pressure. Therefore, at high pressure, the materials stay in the solid state to much higher temperatures than at low pressure. At ambient pressure, Ni_3P has a melting point (~960 ℃), lower than Fe_3P (~1100 ℃) and pure iron (~1500 ℃), which implies that addition of Ni_3P to natural schreibersite lowers the melting point (Lyman, 1973; Okamoto, 2007; Kim et al., 2014).

The presence of Ni in Fe-compounds leads to the loss of ferromagnetic order in Fe_3P because Ni causes decrease of the magnetic moment associated with ferromagnetism of $(Fe, Ni)_3P$ (Gambino et al., 1967; Goto et al. 1977). Ni_3P is less compressible than pure hcp-Fe or iron phosphide phase, including Fe_3P, (Scott et al., 2007; Howard, 2010; Gu et al., 2014). Moreover, first principles calculations on Ni_3P, Fe_3P, and pure hcp-Fe suggest that the shear modulus of Ni_3P is lower than Fe_3P and pure hcp-Fe by approximately 30% and 20% respectively (Zhao et al., 2011; Li et al., 2014; Wu et al., 2015). The higher incompressibility and lower shear modulus of Ni_3P are consistent with the decrease of shear wave velocity of Fe under pressure when adding Ni to Fe-compounds (Lin et al., 2003). Therefore, understanding the high-pressure behavior of this possible core material is important for the interpretation of planetary observations.

5. Conclusions

The compression experiments with Ni_3P up to 50 GPa suggest that unit cell parameters and volume experience two discontinuities at approximately 30 GPa and 40 GPa, which may indicate possible magnetic transitions. The results of this study also illustrate that the c-axis of Ni_3P becomes less compressible above the transition than the a-axis. The discontinuity is sensitive to the stress state and orientation of the crystal in the diamond anvil cell. Moreover, the experiments suggest that substituting Ni into Fe compounds leads to higher incompressibility of the mineral.

Further investigation regarding Fe-Ni alloys, including more direct measurements of magnetic properties are needed to fully explain the observed transitions. Moreover, in order to reliably model core conditions, further measurements will need to be conducted at higher pressure and high temperature.

6. References

Allègre, C. J., Poirier, J. P., Humler, E., & Hofmann, A. W. (1995). The chemical composition of the Earth, *Earth Planet. Earth and Planetary Science Letters*, *134*(3-4), 515–526.

Anderson, D. L. (1989). *Theory of the Earth*. Blackwell scientific publications.

Aronsson, B. (1955). The crystal structure of Ni_3P.(Fe_3P-Type). *Acta Chemica Scandinavica*, *9*, 137-140.

Ashiotis, G., Deschildre, A., Nawaz, Z., Wright, J. P., Karkoulis, D., Picca, F. E., & Kieffer, J. (2015). The fast azimuthal integration Python library: pyFAI. *Journal of applied crystallography*, *48*(2), 510-519.

Birch, F. (1947). Finite elastic strain of cubic crystals. *Physical review*, *71*(11), 809.

Birch, F. (1952). Elasticity and constitution of the Earth's interior. *Journal of Geophysical Research*, *57*(2), 227 -286.

Birch, F. (1978). Finite strain isotherm and velocities for single-crystal and polycrystalline NaCl

at high pressures and 300 K. *Journal of Geophysical Research: Solid Earth*, *83*(B3), 1257-1268.

Board, S. S., & National Research Council. (2007). *The limits of organic life in planetary systems*. National Academies Press.

Bragg, W. H., & Bragg, W. L. (1913). The reflection of X-rays by crystals. Proceedings of the Royal Society of London. Series A, *Containing Papers of a Mathematical and Physical Character*, *88*(605), 428-438.

Brandstätter, F., Koeberl, C., & Kurat, G. (1991). The discovery of iron barringerite in lunar meteorite Y-793274. *Geochimica et Cosmochimica Acta*, *55*(4), 1173-1174.

Britvin, S. N., Kolomenskii, V. D., Boldyreva, M. M., Bogdanova, A. N., Kretser, Y. L., Boldyreva, O. N., & Rudashevskii, N. S. (1999). Nickelphosphide $(Ni, Fe)_3P$, the nickel analog of schreibersite. *ЗАПИСКИ РОССИЙСКОГО МИНЕРАЛОГИЧЕСКОГО ОБЩЕСТВА*.

Britvin, S. N., Rudashevsky, N. S., Krivovichev, S. V., Burns, P. C., & Polekhovsky, Y. S. (2002). Allabogdanite,$(Fe, Ni)_2P$, a new mineral from the Onello meteorite: The occurrence and crystal structure. *American Mineralogist*, *87*(8-9), 1245-1249.

Bryant, D. E., Greenfield, D., Walshaw, R. D., Johnson, B. R., Herschy, B., Smith, C., Pasek M. A., Telford, R., Scowen, I., Munshi, T., Edwards, H. G., Cousins, C.R., Crawford, I. A., & Kee, T. P. (2013). Hydrothermal modification of the Sikhote-Alin iron meteorite under low pH geothermal environments. A plausibly prebiotic route to activated phosphorus on the early Earth. *Geochimica et Cosmochimica Acta*, *109*, 90-112.

Bruker. (2016). APEX3 Crystallography Software Suite.

Buseck, P. R. (1969). Phosphide from metorites: barringerite, a new iron-nickel mineral. *Science*, *165*(3889), 169-171.

Dera, P., Lavina, B., Borkowski, L. A., Prakapenka, V. B., Sutton, S. R., Rivers, M. L., Downs, R. T. & Prewitt, C. T. (2009). Structure and behavior of the barringerite Ni end-member, Ni_2P, at deep Earth conditions and implications for natural Fe-Ni phosphides in planetary cores. *Journal of Geophysical Research: Solid Earth*, *114*(B3).

Dera, P., Lazarz, J. D., & Lavina, B. (2011a). Pressure-induced development of bonding in NiAs type compounds and polymorphism of NiP. *Journal of Solid State Chemistry*, *184*(8), 1997-2003.

Dera, P., Lavina, B., Meng, Y., & Prakapenka, V. B. (2011b). Structural and electronic evolution of Cr_2O_3 on compression to 55 GPa. *Journal of Solid State Chemistry*, *184*(11), 3040-3049.

Dera, P., Zhuravlev, K., Prakapenka, V., Rivers, M. L., Finkelstein, G. J., Grubor-Urosevic, O., Tschauner, O.,Clark, S.M. & Downs, R. T. (2013). High pressure single-crystal micro X-ray diffraction analysis with GSE_ADA/RSV software. *High Pressure Research*, *33*(3), 466-484.

Dewaele, A., Torrent, M., Loubeyre, P., & Mezouar, M. (2008). Compression curves of transition metals in the Mbar range: Experiments and projector augmented-wave calculations. *Physical Review B*, *78*(10), 104102.

Dorfman, S. M., Prakapenka, V. B., Meng, Y., & Duffy, T. S. (2012). Intercomparison of pressure standards (Au, Pt, Mo, MgO, NaCl and Ne) to 2.5 Mbar. *Journal of Geophysical Research: Solid Earth*, *117*(B8).

Dubrovinsky, L. S., Saxena, S. K., Tutti, F., Rekhi, S., & LeBehan, T. (2000). In situ X-ray study of thermal expansion and phase transition of iron at multimegabar pressure. *Physical Review Letters*, *84*(8), 1720.

Dziewonski, A. M., & Anderson, D. L. (1981). Preliminary reference Earth model. *Physics of the earth and planetary interiors*, *25*(4), 297-356.

Fei, Y., Li, J., Bertka, C.M., and Prewitt, C.T. (2000). Structure type and bulk modulus of Fe_3S, a new iron-sulfur compound. *American Mineralogist*, *85*(11-12), 1830-1833.

Gambino, R. J., McGuire, T. R., & Nakamura, Y. (1967). Magnetic Properties of the Iron-Group Metal Phosphides. *Journal of applied physics*, *38*(3), 1253-1255.

Geist, V., Wagner, G., Nolze, G., & Moretzki, O. (2005). Investigations of the meteoritic mineral (Fe, Ni)$_3$P. *Crystal Research and Technology: Journal of Experimental and Industrial Crystallography*, *40*(1-2), 52-64

Golosova, N. O., Kozlenko, D. P., Kichanov, S. E., Lukin, E. V., Liermann, H. P., Glazyrin, K. V., & Savenko, B. N. (2017). Structural and magnetic properties of Cr_2O_3 at high pressure. *Journal of Alloys and Compounds*, *722*, 593-598.

Gonzalez-Platas, J., Alvaro, M., Nestola, F., & Angel, R. (2016) EosFit7-GUI: a new graphical user interface for equation of state calculations, analyses and teaching. *Journal of Applied Crystallography*, *49*(4), 1377-1382

Goto, M., Tange, H., Tokunaga, T., Fujii, H., & Okamoto, T. (1977). Magnetic properties of the

$(Fe_{1-x}M_x)_3P$ compounds. *Japanese Journal of Applied Physics*, *16*(12), 2175.

Gu, T., Wu, X., Qin, S., & Dubrovinsky, L. (2011). In situ high-pressure study of FeP: Implications for planetary cores. *Physics of the Earth and Planetary Interiors*, *184*(3-4), 154-159.

Gu, T., Fei, Y., Wu, X., & Qin, S. (2014). High-pressure behavior of Fe_3P and the role of phosphorus in planetary cores. *Earth and Planetary Science Letters*, *390*, 296-303.

Gull, M., Mojica, M. A., Fernández, F. M., Gaul, D. A., Orlando, T. M., Liotta, C. L., & Pasek, M. A. (2015). Nucleoside phosphorylation by the mineral schreibersite. *Scientific reports*, *5*, 17198.

Hammersley, A. P. (1997). FIT2D: an introduction and overview. European Synchrotron Radiation Facility Internal Report ESRF97HA02T, *68*, 58.

Heinz, D. L., & Jeanloz, R. (1984). The equation of state of the gold calibration standard. *Journal of Applied Physics*, *55*(4), 885-893.

Hemley, R. J., & Mao, H. K. (2001). In situ studies of iron under pressure: New windows on the Earth's core. *International Geology Review*, *43*(1), 1-30.

Howard, J. W. (2010). Finite strain studies of single crystal Fe_3P under high pressures. UNLV Theses/Dissertations/Professional Paper/ Capstones.

Huang, E., Bassett, W. A., & Weathers, M. S. (1988). Phase relationships in Fe-Ni alloys at high pressures and temperatures. *Journal of Geophysical Research: Solid Earth*, *93*(B7), 7741-7746.

Jacobsen, S. D., Holl, C. M., Adams, K. A., Fischer, R. A., Martin, E. S., Bina, C. R., Lin, J. F., Prakapenka, V. B., Kubo, A. & Dera, P. (2008). Compression of single-crystal magnesium oxide to 118 GPa and a ruby pressure gauge for helium pressure media. *American Mineralogist*, *93*(11-12), 1823-1828.

Jun, R. E. N., Wang, J. G., Li, J. F., & Li, Y. W. (2007). Density functional theory study on crystal nickel phosphides. *Journal of Fuel Chemistry and Technology*, *35*(4), 458-464.

Kamada, S., Terasaki, H., Ohtani, E., Sakai, T., Kikegawa, T., Ohishi, Y., Hirao, N., Sata, N., & Kondo, T. (2010). Phase relationships of the Fe-FeS system in conditions up to the Earth's outer core. *Earth and Planetary Science Letters*, *294*(1-2), 94-100.

Kim, T. Y., Son, H. J., Lim, S. K., Song, Y. I., Park, H. S., & Suh, S. J. (2014). Electroless Nickel

Alloy Deposition on SiO2 for Application as a Diffusion Barrier and Seed Layer in 3D Copper Interconnect Technology. *Journal of nanoscience and nanotechnology*, *14*(12), 9515-9524.

Klotz, S., Chervin, J. C., Munsch, P., & Le Marchand, G. (2009). Hydrostatic limits of 11 pressure transmitting media. *Journal of Physics D: Applied Physics*, *42*(7), 075413.

Kozlovsky, Y. A. (1984). The world's deepest well. *Scientific American*, *251*(6), 98-105.

Kuwayama, Y., Hirose, K., Sata, N., & Ohishi, Y. (2008). Phase relations of iron and iron–nickel alloys up to 300 GPa: Implications for composition and structure of the Earth's inner core. *Earth and Planetary Science Letters*, *273*(3-4), 379-385.

Li, J., & Fei, Y. (2003). Experimental constraints on core composition, *Treatise Geochem., 2*, 568.

Li, L. H., Wang, W. L., Hu, L., & Wei, B. B. (2014). First-principle calculations of structural, elastic and thermodynamic properties of Fe–B compounds. *Intermetallics, 46*, 211-221.

Lin, J. F., Heinz, D. L., Campbell, A. J., Devine, J. M., & Shen, G. (2002). Iron-silicon alloy in Earth's core?. *Science*, *295*(5553), 313-315.

Lin, J. F., Struzhkin, V. V., Sturhahn, W., Huang, E., Zhao, J., Hu, M. Y., Alp, E. E., Mao, H. K., Boctor, N., & Hemley, R. J. (2003). Sound velocities of iron-nickel and iron-silicon alloys at high pressures. *Geophysical Research Letters*, *30*(21).

Lin, J. F., Fei, Y., Sturhahn, W., Zhao, J., Mao, H. K., & Hemley, R. J. (2004). Magnetic transition and sound velocities of Fe3S at high pressure: implications for Earth and planetary cores. *Earth and Planetary Science Letters*, *226*(1-2), 33-40.

Litasov, K.D., & Shatskiy, A.F. (2016). Composition of the Earth's core. *Russian Geology and Geophysics*, *57*(1), 22-46

Lyman, T. (1973). Metallography, Structures and Phase Diagrams, Metal Handbook.

Maciá, E., Hernández, M. V., & Oró, J. (1997). Primary sources of phosphorus and phosphates in chemical evolution. *Origins of Life and Evolution of the Biosphere*, *27*(5-6), 459-480.

Mao, H. K., Bell, P. M., Shaner, J. T., & Steinberg, D. J. (1978). Specific volume measurements of Cu, Mo, Pd, and Ag and calibration of the ruby R1 fluorescence pressure gauge from 0.06 to 1 Mbar. *Journal of applied physics*, *49*(6), 3276-3283.

Mao, H. K., Xu, J. A., & Bell, P. M. (1986). Calibration of the ruby pressure gauge to 800 kbar under quasi-hydrostatic conditions. *Journal of Geophysical Research: Solid Earth*, *91*(B5), 4673-4676.

Mao, H. K., Wu, Y., Chen, L. C., Shu, J. F., & Jephcoat, A. P. (1990). Static compression of iron to 300 GPa and $Fe_{0.8}Ni_{0.2}$ alloy to 260 GPa: Implications for composition of the core. *Journal of Geophysical Research: Solid Earth*, *95*(B13), 21737-21742.

Mao, W. L., Campbell, A. J., Heinz, D. L., & Shen, G. (2006). Phase relations of Fe–Ni alloys at high pressure and temperature. *Physics of the Earth and Planetary Interiors*, *155*(1-2), 146-151.

McDonough, W. F.& Sun, S. S. (1995). The composition of the Earth, *Chemical Geology*, *120*(3-4), 223 – 253.

McDonough, W. F. (2014). 3.16–Compositional model for the Earth's core. *Treatise on geochemistry*, 559-577.

Murnaghan, F. D. (1937). Finite deformations of an elastic solid. *American Journal of Mathematics*, *59*(2), 235-260.

Murnaghan, F. D. (1944). The compressibility of media under extreme pressures. *Proceedings of the National Academy of Sciences*, *30*(9), 244-247.

Okamoto, H. (2007). Fe-P (Iron-Phosphorus). *Journal of Phase Equilibria and Diffusion*, *28*(6), 588-588.

Pasek, M. A., & Lauretta, D. S. (2005). Aqueous corrosion of phosphide minerals from iron meteorites: a highly reactive source of prebiotic phosphorus on the surface of the early Earth. *Astrobiology*, *5*(4), 515-535.

Pedersen, A. K. (1981). Armalcolite-bearing Fe-Ti oxide assemblages in graphite-equilibrated salic volcanic rocks with native iron from Disko, central West Greenland. *Contributions to Mineralogy and Petrology*, *77*(4), 307-324.

Poirier, J.P. (1994). Light elements in the Earth's outer core: a critical review. *Physics of the Earth and Planetary Interiors*, *85*(3-4), 319–337.

Pratesi, G., Bindi, L., & Moggi-Cecchi, V. (2006). Icosahedral coordination of phosphorus in the crystal structure of melliniite, a new phosphide mineral from the Northwest Africa 1054 acapulcoite. *American Mineralogist*, *91*(2-3), 451-454.

Prescher, C., Prakapenka, V. B. (2015). DIOPTAS: a program for reduction of two-dimensional X-ray diffraction data and data exploration. *High Pressure Research*, *35*(3), 223-230.

Pritekel, C. (2015). The crystal structure of meteoritic schreibersite: refinement of the absolute crystal structure.

Ringwood, A.E. (1977). Composition of the core and implications for origin of the Earth. *Geochemical Journal*, *11*(3), 111-135.

Rivers, M., Prakapenka, V. B., Kubo, A., Pullins, C., Holl, C. M., & Jacobsen, S. D. (2008). The COMPRES/GSECARS gas-loading system for diamond anvil cells at the Advanced Photon Source. *High Pressure Research*, *28*(3), 273-292.

Rundqvist, S., Hassler, E. & Lundvik, L. (1962). Refinement of Ni_3P Structure. *Acta Chemica Scandinavica, 16(1)*, 242.

Rundqvist, S. (1962). X-Ray Investigations of the Ternary System Fe-P-B. Some Features of the Systems Cr-P-B, Mn-P-B, Co-P-B and Ni-P-B. *Acta Chemica Scandinavica*, *16*, 1-19

Scott, H. P., Huggins, S., Frank, M. R., Maglio, S. J., Martin, C. D., Meng, Y., Santillán, J., Williams, Q. (2007). Equation of state and high-pressure stability of Fe_3P-schreibersite: Implications for phosphorus storage in planetary cores. *Geophysical Research Letters*, *34*(6).

Seagle, C. T., Campbell, A. J., Heinz, D. L., Shen, G., & Prakapenka, V. B. (2006). Thermal equation of state of Fe_3S and implications for sulfur in Earth's core. *Journal of Geophysical Research: Solid Earth*, *111*(B6).

Sheldrick, G. M. (2003). Cell_Now program for unit cell determination. *University of Göttingen: Germany*.

Sheldrick, G. M. (2008a). A short history of SHELX. Acta Crystallographica Section A: *Foundations of Crystallography*, *64*(1), 112-122.

Sheldrick, G. M. (2008b). XPREP Version 2008/2. Bruker AXS Inc., Madison, Wisconsin, USA.

Silvera, I. F., Chijioke, A. D., Nellis, W. J., Soldatov, A., & Tempere, J. (2007). Calibration of the ruby pressure scale to 150 GPa. p*hysica status solidi (b)*, *244*(1), 460-467.

Skála, R., & Drábek, M. (2003). Nickelphosphide from the Vicenice octahedrite: Rietveld crystal structure refinement of synthetic analogue. *Mineralogical Magazine*, *67*(4), 783-792

Skála, R., & Císařová, I. (2005). Crystal structure of meteoritic schreibersite: determination of absolute structure. *Physics and Chemistry of Minerals*, *31*(10), 721-732.

Solé, V. A., & Papillon, E. (2004). Pymca: X-ray spectra visualization and analysis in python. *In NOBUGS 2004 conference, Paul Scherrer Institute, Villigen PSI, Switzerland.*

Steinle-Neumann, G., Stixrude, L., Cohen, R. E., & Gülseren, O. (2001). Elasticity of iron at the temperature of the Earth's inner core. *Nature*, *413*(6851), 57.

Ulff-Møller, F. (1985). Solidification history of the Kitdlit Lens: immiscible metal and sulphide liquids from a basaltic dyke on Disko, central West Greenland. *Journal of Petrology*, *26*(1), 64-91.

Urakawa, S., Matsubara, R., Katsura, T., Watanabe, T., & Kikegawa, T. (2011). Stability and bulk modulus of Ni_3S, a new nickel sulfur compound, and the melting relations of the system Ni-NiS up to 10 GPa. *American Mineralogist*, *96*(4), 558-565.

Wu, J., Chong, X., Zhou, R., Jiang, Y., & Feng, J. (2015). Structure, stability, mechanical and electronic properties of Fe–P binary compounds by first-principles calculations. *RSC Advances*, *5*(100), 81943-81956.

Ye, Y., Prakapenka, V., Meng, Y., & Shim, S. H. (2017). Intercomparison of the gold, platinum, and MgO pressure scales up to 140 GPa and 2500 K. *Journal of Geophysical Research: Solid Earth*, *122*(5), 3450-3464.

Zhao, D., Zhou, L., Du, Y., Wang, A., Peng, Y., Kong, Y., Sha, C., Ouyang, Y., & Zhang, W. (2011). Structure, elastic and thermodynamic properties of the Ni–P system from first-principles calculations. *Calphad*, *35*(3), 284-291.

Zeppenfeld, K., & Jeitschko, W. (1993). Magnetic behaviour of Ni_3P Ni_2P, NiP_3 and the series $Ln_2Ni_{12}P_7$ (Ln= Pr, Nd, Sm, GdLu). *Journal of Physics and Chemistry of Solids, 54*(11), 1527-1531.